

Learning With Constraint Learning: New Perspective, Solution Strategy and Various Applications

Risheng Liu^{ID}, Member, IEEE, Jiaxin Gao^{ID}, Xuan Liu^{ID}, and Xin Fan^{ID}, Senior Member, IEEE

Abstract—The complexity of learning problems, such as Generative Adversarial Network (GAN) and its variants, multi-task and meta-learning, hyper-parameter learning, and a variety of real-world vision applications, demands a deeper understanding of their underlying coupling mechanisms. Existing approaches often address these problems in isolation, lacking a unified perspective that can reveal commonalities and enable effective solutions. Therefore, in this work, we proposed a new framework, named Learning with Constraint Learning (LwCL), that can holistically examine challenges and provide a unified methodology to tackle all the above-mentioned complex learning and vision problems. Specifically, LwCL is designed as a general hierarchical optimization model that captures the essence of these diverse learning and vision problems. Furthermore, we develop a gradient-response based fast solution strategy to overcome optimization challenges of the LwCL framework. Our proposed framework efficiently addresses a wide range of applications in learning and vision, encompassing three categories and nine different problem types. Extensive experiments on synthetic tasks and real-world applications verify the effectiveness of our approach. The LwCL framework offers a comprehensive solution for tackling complex machine learning and computer vision problems, bridging the gap between theory and practice.

Index Terms—Learning with constraint learning, hierarchical optimization, gradient-response, learning and vision applications.

I. INTRODUCTION

IN RECENT years, a plethora of endeavors have emerged to tackle contemporary intricate problems such as Generative Adversarial Network (GAN) and its variants [1], [2], multi-task meta learning [3], [4], hyper-parameter learning [5], [6], and various challenging real-world vision applications [7], [8]. In contrast to these conventional learning paradigms that solely focus on a single learning objective (e.g., classification and regression), these aforementioned modern complex problems often necessitate the simultaneous handling of multiple interrelated learning tasks. For instance, the well-known GANs often require discriminator assisted branches in the process of adversarial

Manuscript received 25 July 2023; revised 18 December 2023; accepted 29 January 2024. Date of publication 9 February 2024; date of current version 5 June 2024. This work was supported in part by the National Key R&D Program of China under Grant 2022YFA1004101, in part by the National Natural Science Foundation of China under Grant U22B2052 and Grant 62027826, and in part by Liaoning Revitalization Talents Program under Grant 2022RG04. Recommended for acceptance by M. P. Kumar. (*Corresponding author: Risheng Liu*)

The authors are with the School of Software Technology, Dalian University of Technology, Dalian, Liaoning 116024, China (e-mail: rsliu@dlut.edu.cn; jiaxin.gao@outlook.com; liuxuan_16@126.com; xin.fan@dlut.edu.cn).

Digital Object Identifier 10.1109/TPAMI.2024.3364157

game [2], [9]. Similarly, multi-task and meta learning introduce task-specific classifiers as supportive sub-tasks to facilitate the acquisition of enhanced generalization representations of meta-features [3], [10]. Hyper-parameter learning involves the construction of simple classifiers as interconnected tasks, aiding the base model in attaining optimal hyper-parameters [11], [12]. Despite the presence of diverse motivations and mechanisms, all these issues encounter the challenge of simultaneously addressing multiple interrelated tasks with coupled structures. This hierarchical coupling induces complexity in the learning process and constitutes the fundamental factor exacerbating the difficulties encountered in problem-solving.

While considerable progresses have been made in various related fields, existing state-of-the-art techniques are all tailored for specific tasks and thus can only solve these different complex problems in isolation. For example, it is challenging to utilize GAN's technique [1] to formulate and address the problem of multi-task meta learning [3]. Fundamental differences also persist in the methodologies employed across various vision applications. More generally, it indeed lacks a unified methodology for revealing the commonalities and addressing the complexity arising from the coupling of multiple sub-tasks.

In the following, this paper endeavors to establish a unified and coherent optimization perspective that explores the intrinsic relationships of these modern complex problems, considering their potential coupling. Termed as Learning with Constraint Learning (LwCL) in this paper, this perspective offers a comprehensive framework for understanding and formulating these problems. Essentially, the LwCL problem can be formulated as follows:

Problem 1: Learning with Constraint Learning (LwCL) represents an innovative learning mechanism, distinguished by a hierarchical arrangement of two interconnected learning tasks. Within LwCL, the fulfillment of the primary objective task (referred to as the Objective Learner or OL) relies upon the successful completion of a lower-level learning task (referred to as the Constraint Learner or CL).¹ This hierarchical structure endows the learning process with added depth, as the CL acts as a constraint that must be satisfied, effectively guiding and shaping the optimization process towards the attainment of the overarching objective. Through this nested hierarchy, LwCL enhances the learning process, fostering a more structured and directed approach to achieving the desired learning outcome.

¹The detailed concepts and applications of this framework will be presented in Sections III and IV, respectively.

In essence, LwCL embodies a nested hierarchy of learning tasks, where each subtask contributes to the accomplishment of the overarching objective. This intricate nested framework adds complexity to the learning process and requires a more sophisticated approach to problem-solving. It can be challenging because the optimization process must balance the competing objectives of completing the subtasks at each layer while also optimizing the overall objective of the entire system. From a macroscopic perspective, by introducing this constraint-based hierarchical structure, LwCL can serve as a unified methodology, capable of revealing commonalities and addressing a range of complex learning problems.

Based on the above analysis, the primary objective of this paper is to present a unified perspective, termed LwCL, which aims to reinterpret and elucidate the underlying mechanisms of modern complex problems. Building upon this foundation, we have developed a generic hierarchical optimization framework, encompassing reformulation and algorithmic components, to unveil the potential coupling constraints among multiple tasks. Additionally, leveraging the concept of dynamic best response, we have employed an outer-product-based Hessian approximation technique to devise a rapid solving strategy from the standpoint of implicit gradients. This approach enables accurate tracing of the gradient feedback dynamics between the OL and the CL, thereby yielding unprecedented advancements in training stability and performance. Importantly, our proposed method exhibits remarkable flexibility and adaptability, as it can be seamlessly integrated into a diverse range of contemporary complex learning problems, owing to the inherent tolerance of the constraint learning paradigm towards the requirements of the objective function. We also demonstrate that our proposed framework can efficiently address a wide range of LwCL applications in the fields of learning and vision, including three categories of problems, with a total of nine different types.

Our contributions can be summarized as follows:

- From a comprehensive and in-depth point of view, we introduce a unified perspective, termed as Learning with Constraint Learning (LwCL), to analyze, reformulate, and address a wide array of complex learning problems that exhibit underlying coupled relationships in the domains of machine learning and computer vision.
- We propose a hierarchical optimization framework that effectively formulates the potential dependencies and uncovers the inherent coupling among multiple tasks within LwCLs. This framework facilitates precise optimization of the two learning tasks through a synergistic and interactive approach, incorporating the proposed gradient-response feedback.
- To alleviate high computational complexity issues associated with naive learning strategy, we design an implicit gradient scheme with outer-product Hessian approximation as fast solution strategy to efficiently solve the nested optimization process, which is more computation-friendly and suitable for diverse high-dimensional large-scale real-world applications.
- We demonstrate that LwCL can efficiently address a wide range of modern complex learning and vision applications,

including three categories of problems, with a total of nine different types. The versatility and effectiveness of our proposed LwCL framework is verified through extensive experiments on both synthetic tasks and real-world applications.

II. REVIEW OF RELATED WORKS WITHIN LwCL

Based on Problem 1, we now proceed to comprehensively understand and (re)formulate existing modern works from the unified perspective of LwCL. Specifically, we categorize these works into three classes, including Adversarial Learning (AL), Auxiliary with Related Tasks (ART), and Task Divide and Conquer (TDC), utilizing the lens of LwCL.

AL-Type Applications: As one of the most popular LwCTs, AL-based methods exhibit a strong ability to model specific data distribution by addressing the assisted discriminative tasks via a dynamic adversarial game. OL and CL can be regarded as generator learning and discriminator learning, respectively. For example, vanilla GAN [1], as a discriminator-assisted learning problem, can be interpreted as a dynamic adversarial game that greedily finds the solution of the minmax formula through an alternating iterative strategy. Metz et al. [13] proposed the idea that gradients can be back-propagated through the unrolled optimization procedure in a differentiable way to address the challenges of unstable optimization. Accordingly, various variants of loss types and regulation (i.e., second-order gradient loss [13], Hinge loss [14], and Lipschitz penalty [15]) also appear in the optimization objectives of GAN-variants. Nonetheless, these methods still suffer from poor generation quality, training oscillations, and other challenges that have not been fully addressed. In addition to the narrowly defined GANs and their variants, a series of adversarial vision tasks in cutting-edge areas, such as image generation [2], [16], [17], [18], style transfer [9], [19] and imitation learning [20], [21] have risen in recent years. These problems employ different task-specific losses and strategies to mitigate the reconstruction discrepancy between different image domains in training process. For example, Zhu et al. [22] constructed bi-directional cycle generative-discriminative architecture and cycle consistency loss to complete cross-domain style transfer. In reinforcement learning, Pfau et al. [23] treated the discriminator as a regression task providing scalar values rather than a binary classifier and opened up new avenues of research by treating adversarial learning programs as an actor-critic problem. Despite the good intentions of these approaches, existing AL-based strategies still suffer from several major challenges, such as training instability, oscillations and mode collapse. The underlying reason is the inability of learning mechanisms that rely on alternating iterations to accurately portray the intrinsically complex dynamics between the considered task and the introduced adversarial task. Therefore, we proceed to present new mathematical tools to model and solve such AL-type problems.

ART-Type Applications: In recent decades, a category of typical learning tasks towards sophisticated applications have addressed considered learning tasks with related auxiliary learning devices, named auxiliary with related tasks, such as medical

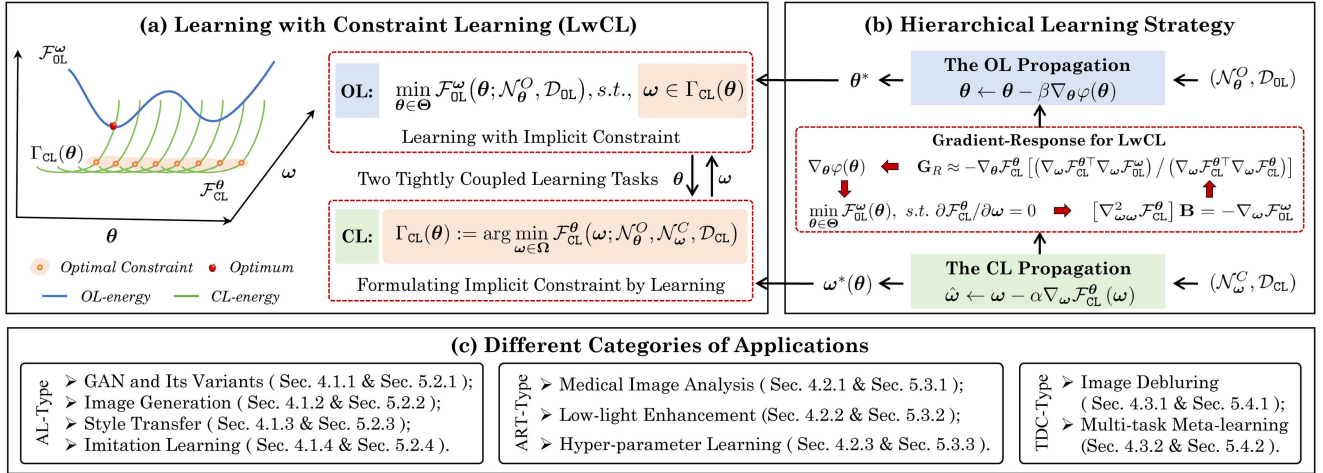


Fig. 1. Overview of the proposed method. In (a) we present a novel LwCL perspective to comprehensively investigate and address these contemporary complex problems with underlying coupling relationships in a unified manner. To effectively resolve the nested optimization process, (b) introduces a specially designed dynamic gradient-response solution strategy tailored for LwCL. Lastly, (c) provides a comprehensive enumeration of nine major problem categories spanning three broad application areas that our method can effectively tackle. Please notice that the diagram in (a) is just a simplified illustration for our LwCL mechanism. However, in real applications, both OL and CL tasks will pose significantly higher complexity and challenges, such as non-convex learning problems.

image analysis (i.e., medical image registration and segmentation [24], [25], [26], [27] and low-light image enhancement [28], [29]) and hyper-parameter learning [5], [11], [12], [30], [31]. OL and CL can be regarded as objective learning task and auxiliary learning task, respectively. For example, in the spirit that medical image registration can provide more label information for one-shot image segmentation, Xu et al. [7] developed a joint model for simultaneous image registration and segmentation. For low-light scenes, Xue et al. [29] proposed to introduce additional detection and segmentation models to assist the low-light enhancement task. Actually, these approaches often generally rely on naive empirical strategies (i.e., alternate learning) to solve the problem and often suffer from disadvantages such as low training efficiency, low performance, and poor generalization. Similarly, in order to assist the base model for obtaining optimal hyper-parameters, hyper-parameter learning usually introduces simple classifiers that contain only a few fully connected layers as auxiliary tasks, with first-order gradient based algorithms [5], [30]. However, such methods possess a high algorithmic complexity and are usually limited to low-dimensional data scenarios. Overall, an in-depth exploration focusing on how to uniformly and efficiently formulate and address these ART-type tasks is essential and necessary.

TDC-Type Applications: There is another class of learning task construction ideas, i.e., dividing a complete learning process into multiple subtask learning processes, called task divide and conquer, with typical applications such as image deblur [8], [32] and multi-task meta learning [3], [4], [6], [33], [34]. OL and CL can be regarded as meta-feature/prior learning and task-specific classifier/fidelity learning, respectively. For example, meta-feature learning methods [4], [33] generally separated the network structure into meta-feature extraction modules and task-specific modules. The latter guides better learning of generalization representations of meta-features by constructing losses for multiple different tasks. Admittedly, the above methods

are usually confined to small-scale, low-dimensional simulation scenarios, and still suffer from various unsolved challenges such as training instability and computational inefficiency for real-world high-dimensional applications. For image deblur task, Zhang et al. [35] proposed semi-quadratic split-based deep unrolling method to enhance deblurred images, divided into the fidelity learning and a prior learning subproblems. Among them, the prior learning task introduce a plug-and-play denoiser. Unfortunately, the fixed pre-trained denoiser, lacks generalization applicability to various complex scenarios. In the subsequent sections, we will develop a deeper understanding, modeling and solving such TDC-type problems from the LwCL perspective.

III. LEARNING WITH CONSTRAINT LEARNING

In this section, we endeavor to establish a comprehensive hierarchical optimization framework and a dynamic best response-based fast solution strategy that enable a unified formulation and resolution of various types of LwCL problems. The overall framework is depicted in Fig. 1. In (a), we introduce a novel perspective to comprehensively investigate and address contemporary complex problems (i.e., AL, ART and TDC) in a unified manner. To effectively handle the nested optimization process, (b) illustrates a comprehensive hierarchical optimization framework that aims to redefine and reformulate LwCLs, and proposes a specially designed gradient-response solution strategy tailored specifically for LwCL (as denoted by the dashed rectangle). Finally, (c) provides a comprehensive enumeration of nine major problem categories across three broad application areas that our method can effectively tackle.

A. Hierarchical Optimization Formulation for LwCL

Our investigation is centered around contemporary and intricate LwCL problems, as delineated in Problem 1. Specifically, we regard that the essence of LwCL lies in the construction of

an OL, denoted as \mathcal{N}_θ^O with parameterization θ , which aims to optimize the performance of the desired objective learning task, such as generator learning or meta-feature learning. This endeavor can be expressed as an optimization problem with respect to θ , whereby the OL energy \mathcal{F}_{OL} encapsulates the optimization objective base on the OL dataset \mathcal{D}_{OL} .

Given the inherent complexities in directly solving the OL, it is customary to introduce multiple interrelated learning tasks in the form of auxiliary CL, denoted as \mathcal{N}_ω^C with parameterization ω , to assist the overarching objective of OL. To elucidate the aforementioned notion, we generally introduce the more abstract formulation of energy-constrained learning, which is expressed as

$$\min_{\theta \in \Theta} \mathcal{F}_{OL}^\omega(\theta; \mathcal{N}_\theta^O, \mathcal{D}_{OL}), \text{ s.t., } \omega \in \Gamma_{CL}(\theta), \quad (1)$$

where $\Gamma_{CL}(\theta)$ denotes the optimal constraint with respect to ω . Due to the tight coupling and potential dependency between the two variables, combined with the difficulty in accurately determining $\Gamma_{CL}(\theta)$, the aforementioned problem in (1) becomes extremely complex.

Given this, we introduce a learning modeling approach with constraints that characterizes the optimization process concerning the variable ω . This auxiliary learning task can likewise be framed as an optimization problem, wherein the CL energy \mathcal{F}_{CL}^θ characterizes the performance of CL with variable ω , formulated as

$$\Gamma_{CL}(\theta) := \arg \min_{\omega \in \Omega} \mathcal{F}_{CL}^\theta(\omega; \mathcal{N}_\theta^O, \mathcal{N}_\omega^C, \mathcal{D}_{CL}). \quad (2)$$

By combining (1) and (2), we observe that, the intrinsic hierarchical relationship between the two learners (i.e., \mathcal{N}_θ^O and \mathcal{N}_ω^C) is explicitly encoded by the task-specific energy functions (i.e., \mathcal{F}_{OL}^ω and \mathcal{F}_{CL}^θ).² Furthermore, it is worth noting that the energy functions \mathcal{F}_{OL}^ω (or \mathcal{F}_{CL}^θ) : $\mathbb{R}^m \times \mathbb{R}^n \rightarrow \mathbb{R}$ are continuous, while the set $\Omega \subseteq \mathbb{R}^n$ represents a nonempty feasible region, and $\Theta \subseteq \mathbb{R}^m$ denotes the feasible set for the variables. In this context, we refer to θ and ω as the outer-level (or OL-level) variables and \mathcal{F}_{OL}^ω and \mathcal{F}_{CL}^θ as the outer-level (or OL-level) energy and inner-level (or CL-level) energy, respectively. Building upon the principles of Stackelberg game theory, we strive to present a robust hierarchical optimization framework, serving as a novel mathematical instrument to explicitly inscribe the coupling dependencies of two key players.

Inherently, a notable asymmetry is observed between the two levels of learning tasks, where \mathcal{F}_{CL}^θ assumes the role of a constraint upon \mathcal{F}_{OL}^ω , facilitating the derivation of optimal feedback $\omega(\theta)$ to be passed onto the core optimization objective. This dynamic constrained learning process entails a high degree of interdependence between the variables θ and ω , such that every incremental update of θ is inevitably influenced by the state of ω . For further understanding, (1) and (2) can be regarded as a bi-level optimization problem concerning two variables, where the OL-level and CL-level functions correspond to the upper-level and lower-level functions, respectively. The curve

²The detailed design of \mathcal{F}_{OL}^ω and \mathcal{F}_{CL}^θ in specific applications will be presented in Section IV.

schematic in Fig. 1(a) illustrates a simple visualization of a bi-level optimization problem. To address practical applications in high-dimensional real-world scenarios, we proceed to propose a rapid and efficient solution strategy depicted in Fig. 1(b). This strategy is distinguished by its dynamic best-response approach, with arrows illustrating the flow of gradient updates pertinent to two sub-problems.

B. Solution Strategy With Gradient-Response

Commencing from the dynamic gradient-response, we further define the value-function $\varphi(\theta)$, leading us to the minimization problem, $\min_\theta \varphi(\theta) := \mathcal{F}_{OL}^\omega(\theta, \omega(\theta))$. Progressing further, the key to resolving this problem lies in computing the gradient of the OL optimization objective:

$$\nabla_\theta \varphi(\theta) = \nabla_\theta \mathcal{F}_{OL}^\omega(\theta, \omega(\theta)) + \underbrace{\nabla_\omega \mathcal{F}_{OL}^\omega(\theta, \omega(\theta)) \nabla_\theta \omega(\theta)}_{\mathbf{G}_R}. \quad (3)$$

Notably, the direct gradient term $\nabla_\theta \mathcal{F}_{OL}^\omega(\theta, \omega)$ showcases a straightforward reliance on the OL variable θ and can be readily obtained through simple computations in practice. Conversely, the second gradient term, denoted as \mathbf{G}_R poses challenges in its calculation due to the varying rate of $\omega(\theta)$ with respect to θ . Nonetheless, \mathbf{G}_R accurately captures the best response gradient (in connection with $\nabla_\omega \mathcal{F}_{CL}^\theta$ and $\nabla_\theta \mathcal{F}_{CL}^\theta$) between the two learning tasks and assumes a pivotal role in optimizing LwCLs. Essentially, equipped with (3), the gradient of \mathcal{N}_ω^C can be dynamically and accurately back-propagated to \mathcal{N}_θ^O at each iteration, effectively aiding in the optimization of its parameters.

Undoubtedly, evaluating the exact best response gradient of (3) poses significant computational challenges for most existing strategies, particularly when the dimensions of ω and θ are high. To address this challenge, we leverage implicit methods, which offer a direct and precise estimation of the optimal gradient. Inspired by the implicit function theorem, we derive the following equation based on the best response gradient, i.e., $\partial \mathcal{F}_{CL}^\theta / \partial \omega = 0$. In contrast to the solution strategy, the best response gradient is then substituted with an implicit equation, wherein $\nabla_\theta \omega(\theta)$ is derived as:

$$\nabla_\theta \omega(\theta) = - [\nabla_\omega^2 \mathcal{F}_{CL}^\theta(\theta, \omega(\theta))]^{-1} \nabla_{\omega\theta}^2 \mathcal{F}_{CL}^\theta(\theta, \omega(\theta)). \quad (4)$$

Considering the formidable challenges associated with computing the Hessian and its inverse, we propose a fast solution strategy by simplifying the second derivative to the first derivative, enabling the calculation of the best response Jacobian. This strategy involves two key computational steps: implicit gradient estimation and outer-product approximation.

Implicit Gradient Estimation: To circumvent the direct calculation of multiple Hessian products and their inversions, we introduce a linear solver system \mathbf{B} based on (4), allowing us to avoid the complexity associated with computing \mathbf{G}_R . Consequently, the indirect response gradient can be reformulated as:

$$\mathbf{G}_R = [\nabla_{\omega\theta}^2 \mathcal{F}_{CL}^\theta]^\top \mathbf{B}, \text{ where } [\nabla_{\omega\omega}^2 \mathcal{F}_{CL}^\theta] \mathbf{B} = -\nabla_\omega \mathcal{F}_{OL}^\omega, \quad (5)$$

where $(\cdot)^\top$ denotes the transposition operation. Through this formulation, \mathbf{G}_R is solely dependent on the first-order condition, effectively decoupling the computational burden from the solution trajectory of the constrained sub-task. This decoupling greatly alleviates the pressure of propagating the backward gradient in the constrained dynamics.

However, it is worth noting that the calculation of second-order derivatives in \mathbf{G}_R remains intractable. The pressing need to approximate the repeated computation of two Hessian matrices, $\nabla_{\omega\omega}^2 \mathcal{F}_{\text{CL}}^\theta$ and $\nabla_{\omega\theta}^2 \mathcal{F}_{\text{CL}}^\theta$, has led to the emergence of the concept of outer-product approximation.

Outer-Product Approximation: To further suppress the complexity of constrained optimization, we consider replacing the original Hessian operation with the Gauss-Newton strategy and introduce two corresponding outer products, as follows:

$$\nabla_{\omega\omega}^2 \mathcal{F}_{\text{CL}}^\theta \approx \nabla_\omega \mathcal{F}_{\text{CL}}^\theta \nabla_\omega \mathcal{F}_{\text{CL}}^{\theta\top}, \quad \nabla_{\omega\theta}^2 \mathcal{F}_{\text{CL}}^\theta \approx \nabla_\omega \mathcal{F}_{\text{CL}}^\theta \nabla_\theta \mathcal{F}_{\text{CL}}^{\theta\top}. \quad (6)$$

By separating the gradient, this approach converts the highly complex second-order derivative into a simple product operation involving the first-order derivative, which significantly reduces the algorithm's complexity, especially in terms of memory consumption. By combining (5)–(6), we establish the nonlinear least squares problem by approximating the Gauss-Newton formula. Plugging into the (5), thus we can obtain

$$(\nabla_\omega \mathcal{F}_{\text{CL}}^\theta \nabla_\omega \mathcal{F}_{\text{CL}}^{\theta\top})^2 \mathbf{B} \approx -(\nabla_\omega \mathcal{F}_{\text{CL}}^\theta \nabla_\omega \mathcal{F}_{\text{CL}}^{\theta\top})^\top \nabla_\omega \mathcal{F}_{\text{OL}}^\omega. \quad (7)$$

To over simplify, we can express \mathbf{B} with \mathbf{M} as follows $\mathbf{B} = \mathbf{M}(\nabla_\omega \mathcal{F}_{\text{CL}}^{\theta\top} \nabla_\omega \mathcal{F}_{\text{CL}}^\theta) \nabla_\omega \mathcal{F}_{\text{OL}}^\omega$, where $\mathbf{M} = [\nabla_\omega \mathcal{F}_{\text{OL}}^\omega (\nabla_\omega \mathcal{F}_{\text{CL}}^{\theta\top} \nabla_\omega \mathcal{F}_{\text{CL}}^\theta) \nabla_\omega \mathcal{F}_{\text{CL}}^{\theta\top}]^{-1}$. Ultimately, we obtain an approximate representation of the response gradient \mathbf{G}_R as follows:

$$\mathbf{G}_R \approx -\nabla_\theta \mathcal{F}_{\text{CL}}^\theta [(\nabla_\omega \mathcal{F}_{\text{CL}}^{\theta\top} \nabla_\omega \mathcal{F}_{\text{OL}}^\omega) / (\nabla_\omega \mathcal{F}_{\text{CL}}^{\theta\top} \nabla_\omega \mathcal{F}_{\text{CL}}^\theta)]. \quad (8)$$

Drawing upon the aforementioned derivations, we can succinctly outline the comprehensive solution strategy as Algorithm 1. During the training phase, given the current parameter set θ , we initiate the optimization of ω based on the objective function $\mathcal{F}_{\text{CL}}^\theta$, iteratively refining it to approximate the dynamic best response, denoted as $\hat{\omega}(\theta) \approx \omega(\theta)$. Subsequently, we propagate the updated $\omega(\theta)$ to $\mathcal{F}_{\text{OL}}^\omega$, where we calculate the response gradient \mathbf{G}_R utilizing our proposed implicit gradient strategy (i.e., (8)). This computed gradient, in turn, facilitates the iterative update of θ until convergence is attained.

C. Discussion

By fundamentally elucidating the underlying coupling relationships among multiple learning tasks in complex problems, our methodology provides a comprehensive understanding of their intricate interplay. Moreover, the proposed dynamic best response based solution strategy not only showcases scalability, adaptability, and generalizability but also empowers its application across a broad spectrum of large-scale, high-dimensional real-world scenarios.

Unveiling the Intrinsic Coupling Relationships for Complex Learning Problems: Traditional approaches in the past have often relied on task-specific methodologies, limiting their

Algorithm 1: Fast Solution Strategy for LwCL

Input: Initialization of θ, ω , energy functions $\mathcal{F}_{\text{OL}}^\omega$ and $\mathcal{F}_{\text{CL}}^\theta$, and other essential hyper-parameters.

Output: The optimal parameters θ^* and ω^* .

- 1: **while** not converge **do**
 - 2: % CL – level variable probe
 - 3: Obtain an approximation $\hat{\omega}$ to ω by updating
 $\hat{\omega} \leftarrow \omega - \alpha \nabla_\omega \mathcal{F}_{\text{CL}}^\theta(\omega)$ (α : learning rate).
 - 4: % OL – level variable probe
 - 5: Calculate the response gradient \mathbf{G}_R with $\hat{\omega}$ and the
 current θ , according to (8).
 - 6: Calculate $\nabla_\theta \varphi(\theta)$ with \mathbf{G}_R by (3).
 - 7: Update $\theta \leftarrow \theta - \beta \nabla_\theta \varphi(\theta)$ (β : learning rate).
 - 8: **end while**
 - 9: **return** θ^* and ω^* .
-

generalization capabilities and hindering their adaptability to different tasks. Moreover, accurately capturing the interdependencies between multiple related learning tasks has proven challenging due to the empirical nature of designing learning strategies. Hence, the need for a unified framework arises, one that can reconcile diverse modeling approaches and explore the inherent connections among these tasks. The LwCL framework tackles these challenges by explicitly considering the nested structure of learning tasks. Its hierarchical optimization framework provides a profound understanding of the potential coupling relationships among tasks, allowing for accurate characterization. Additionally, the framework offers flexibility in integrating various task constraints, rendering it suitable for addressing a wide array of complex learning problems. By leveraging its hierarchical structure, LwCL can act as a unified methodology for uncovering coupled commonalities in various complex learning problems and providing accurate forms for modeling multiple interrelated sub-tasks.

Implicitly-Derived Fast and Efficient Solution Strategy: Indeed, the most straightforward idea towards real-world vision applications is to employ alternating iterative algorithms, where one component is fixed while the other is optimized. While the alternating iterative mechanism exhibits sound design principles, it often leads to a fragmentation between the two learning tasks in practical implementations. Specifically, in (3), conventional alternating methods directly overlook the computation of the coupling term \mathbf{G}_R , thereby disregarding the gradient feedback from CL to OL during the back-propagated process. In contrast, our proposed method addresses this limitation by emphasizing the collaborative synergy between the CL and OL, which is unattainable in traditional alternating approaches. Our proposed solution strategy accurately computes the optimal gradient-response during each iteration of the back-propagation, ensuring a more stable and expeditious convergence in the learning process. In addition to the aforementioned intuitive solutions, the development of bi-level optimization methods capable of performing gradient-based explicit and implicit algorithms through automatic differentiation holds significance [36]. Nevertheless, classical first-order gradient-based algorithms

typically suffer from high complexity and low operational efficiency due to the computation of the recursive or Hessian gradient for \mathbf{G}_R , rendering them impractical for high-dimensional complex real-world scenarios.

We would like to emphasize that our proposed fast solution strategy accurately computes the gradient-response \mathbf{G}_R . Furthermore, it exhibits significant superiority over state-of-the-art gradient-based bi-level optimization methods, particularly in terms of convergence speed and computational complexity. In regards to computational complexity, Algorithm 1 circumvents the need for unfolded recurrent iterations or Hessian inversions for \mathbf{G}_R , thereby avoiding any computations involving Hessian- or Jacobian-vector products. The complexity of our strategy primarily stems from computing the first-order gradient. Considering that the calculation of the function's first derivative and the Hessian-vector product share similar time and space complexity, our proposed approximate method simplifies the process of computing the gradient-response \mathbf{G}_R to evaluating the first-order derivative a few fixed times. In the subsequent experimental section, we undertake a comprehensive set of numerical and real experiments to compare various traditional gradient-based bi-level optimization methods and our fast solution strategy. Through these experiments, we aim to substantiate the exceptional performance of our strategy, specifically in terms of convergence speed and memory utilization. More details on the comparative mechanisms can be found in Section V.

IV. APPLICATIONS OF LWCL

In this section, we provide an elaborate discussion on the versatility of our proposed framework as a general methodology, which can be seamlessly applied to a diverse array of LwCL applications, spanning domains such as AL, ART and TDC within the realms of vision and learning. By applying our framework to these diverse applications, we aim to demonstrate its broad applicability and effectiveness across different domains and tasks.

A. AL-Type Applications

In the realm of AL-type LwCL applications, our focus lies on the introduction various discriminator learning tasks \mathcal{N}_ω^C to assist with the generator learning tasks \mathcal{N}_θ^O . We emphasize that CL entails the incorporation of discriminators (potentially multiple), classifiers, and critics, each equipped with specialized architectures designed to address diverse applications within the realms of vision and learning. As for the constraint energy function $\mathcal{F}_{\text{CL}}^\theta$, its fundamental concept lies in establishing the relationship between the output distribution of \mathcal{N}_θ^O and the distribution of the desired solution for \mathcal{N}_ω^C . In the subsequent discussion, we primarily delve into four prominent categories of representative applications, namely vanilla GAN, image generation, style transfer and imitation learning, which serve as exemplars to showcase the versatility of our framework and its efficacy in these domains.

1) *GAN and Its Variants*: Formally, the learning process of GAN can be conceptualized as the minimization of a distance metric, denoted as "Distance", between the generated

distribution P_G and the data distribution P_{data} , represented as \min "Distance"(P_G, P_{data}). Under the standard definition, vanilla GAN dynamics advocate the incorporation of an auxiliary discriminator D to facilitate the training of the generator G through an alternating learning strategy, seeking to minimize the divergence in the objective $\min_G \max_D \mathcal{V}(G, D)$. In essence, as the most representative instance of LwCL, it can be formulated as a dynamically coupled game process, expressed as $\mathcal{V}[G(\theta), D(\omega)] = \mathcal{F}_{\text{OL}}^\omega(\theta) = -\mathcal{F}_{\text{CL}}^\theta(\omega)$.

By employing an alternating direction iteration strategy, the original learning strategy establishes two gradient flows using gradient descent: $\omega_{t+1} \leftarrow \omega_t - \nabla_\omega \mathcal{F}_{\text{CL}}^\theta(\omega_t)$ and $\theta_{t+1} \leftarrow \theta_t - \nabla_\theta \mathcal{F}_{\text{OL}}^\omega(\theta_t)$. This leads to two independent optimization branches for ω and θ that proceed in parallel. However, the optimization of the generator depends on the discriminator's parameters from the previous step, rather than the current step. This inaccurate approximation fails to capture the coupled best response gradient term depicted in (3). In contrast, our LwCL framework accurately formulates and characterizes the potential dependency of θ on the current ω . Consequently, the optimization of the discriminator can be described by an exact estimated dynamic best response, which is then dynamically back-propagated to the optimization process for the generator dynamics. In light of these considerations, our proposed framework fundamentally circumvents the occurrence of training instabilities and mitigates mode collapse issues. To validate its effectiveness in addressing these challenges, we conduct a comprehensive set of experiments in Section V, which showcase the results of these experiments and provide compelling support for the effectiveness of our framework.

2) *Image Generation*: Image generation aims to generate intricate and diverse images from compact seed inputs. Existing research focuses on developing diverse generative models, but they often encounter challenges during model training and require manual tuning techniques to mitigate mode collapse issues. With the versatility of our proposed framework, we apply our learning strategy to state-of-the-art generative model architectures. Specifically, we introduce different constrained objectives, referred to as CL energy functions $\mathcal{F}_{\text{CL}}^\theta$, such as binary cross-entropy loss, least squares loss and 1-Lipschitz limit-loss with spectral norm. These objectives correspond to discriminators with different network structures. Remarkably, our LwCL framework seamlessly integrates into various advanced GAN variants without necessitating architectural modifications or loss selection changes, thereby consistently enhancing performance. In Section V, we present comprehensive experimental results to demonstrate the effectiveness and efficiency of our LwCL framework. These results showcase more stable training performance and improved generalization capabilities, substantiating the practical benefits of our approach.

3) *Style Transfer*: Style transfer aims to impose style constraints by optimizing the adversarial loss between two distinct datasets, while ensuring content preservation through reverse transformations. Drawing inspiration from the circular generative adversarial architecture proposed in Zhu et al. [9], we establish a bidirectional adversarial learning framework to guide the style transfer task. Specifically, by creating a cyclic mapping

between two domains, denoted as X and Y , we introduce two generators, namely G_1 and G_2 , along with two discriminators, denoted as D_X and D_Y . To capture the complexity of unsupervised learning, we design two components for our loss functions: the least squares loss \mathcal{L}_{GAN} and cycle consistency loss \mathcal{L}_{cyc} , which account for the original input and the output after inverse transformation. Within our LwCL framework, we define the objective learner \mathcal{N}_θ^O and the constraint learner \mathcal{N}_ω^C as the two generators with parameters θ and the two discriminative classifiers with parameters ω , respectively. The OL and CL objectives can then be expressed as $\mathcal{F}_{OL}^\omega = -\mathcal{F}_{CL}^\theta = \mathcal{L}(G_1, G_2, D_X, D_Y) = \mathcal{L}_{GAN}(G_1, D_Y, X, Y) + \mathcal{L}_{GAN}(G_2, D_X, Y, X) + \mathcal{L}_{cyc}(G_1, G_2)$. More details on the setup of the forward and backward cyclic consistency functions can be found in the experimental section.

4) Imitation Learning: Imitation learning endeavors to achieve optimal decision-making by interacting with the environment and acquiring knowledge from experiences. The objective of imitation learning is to simultaneously learn a state-action value function, denoted as Q^π , which predicts the expected discounted cumulative reward, and an optimal policy that aligns with the value function. Formally, we have: $Q^\pi(s, a) = \mathbb{E}_{s_{i+j} \sim \mathcal{P}, r_{i+j} \sim \mathcal{R}, a_{i+j} \sim \pi} (\sum_{k=0}^{\infty} \gamma^k r_{i+j} | s_i = s, a_i = a)$, where \mathcal{P} and \mathcal{R} denote dynamics of the environment and reward function, respectively. Here, s and a are the state and action, i and j refer to the i -th and j -th steps in the learning process. Within our LwCL paradigm, the actor and critic correspond to the objective learner \mathcal{N}_θ^O and constraint learner \mathcal{N}_ω^C , respectively. Let θ denote the parameters of the state-action value-function and ω denote the parameters of the policy π . The expressions for \mathcal{F}_{OL}^ω and \mathcal{F}_{CL}^θ are given by: $\mathcal{F}_{OL}^\omega := \mathbb{E}_{s_i, a_i \sim \pi} [\text{div}(\mathbb{E}_{s_{i+1}, a_{i+1}, r_{i+1}}(D_Q) \| Q(s_i, a_i))]$, and $\mathcal{F}_{CL}^\theta := -\mathbb{E}_{s_0 \sim p_0, a_0 \sim \pi} Q^\pi(s_0, a_0)$, where $\text{div}(\cdot \| \cdot)$ represents any divergence and $D_Q = r_{i+1} + \gamma Q(s_{i+1}, a_{i+1})$. For specific settings of the state-action value function, please refer to the experimental section.

B. ART-Type Applications

As mentioned previously, ART-type LwCL tasks solving sophisticated applications have introduced related tasks as auxiliary CL devices to augment the considered OL tasks. In the subsequent subsections, we delve into three specific applications that leverage auxiliary task constraints: medical image analysis, low-light image enhancement and hyper-parameter learning.

1) Medical Image Analysis: Medical image analysis involves the extraction of anatomical structures or lesions from medical images. Drawing inspiration from the concept that learning registration can provide additional pseudo-labeled training data to assist segmentation [24], we leverage our LwCL framework to dynamically address inter-task dependencies. In our framework, the registration process serves as the objective learner \mathcal{N}_θ^O , while the segmentation process acts as the constraint learner \mathcal{N}_ω^C . Building upon a base model [7], we incorporate a semantic consistency constraint into the segmentation task. Under our LwCL framework, the OL procedures for the registration task can be formulated as $\mathcal{F}_{OL}^\omega :=$

$\min_\theta \mathcal{L}_{reg}(\mathcal{N}_R(I_{mov}, I_{fix}, \theta))$, where \mathcal{N}_R represents the registration network with learnable parameters θ , and I_{mov} and I_{fix} denote the moving image and fixed image, respectively. Subsequently, by obtaining the warped image I_{war} , the CL procedures for the segmentation task can be formulated as $\mathcal{F}_{CL}^\theta := \min_\theta \mathcal{L}_{seg}(\mathcal{N}_S(\mathcal{N}_R(I_{war}, I_{fix}, \theta)); \omega)$, where \mathcal{N}_S represents the segmentation network with learnable parameters ω . Please refer to the experimental section in Section VI for specific details on the settings of the loss functions.

2) Low-Light Image Enhancement: Low-light image enhancement aims to reveal hidden information in dark areas to improve overall image quality. Drawing on the principles of the Retinex theory, we delve into the impact of downstream perceptual tasks, such as object detection, on the performance of upstream enhancement tasks. Guided by this concept, we construct a low-light enhancement network, inspired by recent advancements [37], as our objective learner \mathcal{N}_θ^O . Furthermore, we introduce a face detector proposed by [38] as an auxiliary constraint learner \mathcal{N}_ω^C . Within our LwCL framework, we employ the unsupervised illumination learning loss $\mathcal{F}_{OL}^\omega := \mathcal{L}_p + \mathcal{L}_s$ as the OL function. Here, \mathcal{L}_p and \mathcal{L}_s represent the pixel fidelity term and smoothness term, respectively, which evaluate the performance of the upstream enhancement task. For the energy function \mathcal{F}_{CL}^θ of the constraint learner, we introduce the anchor-based multi-task loss and progressive anchor loss to assess the detection performance, defined as: $\mathcal{F}_{CL}^\theta := \mathcal{L}_{SSL}(a) + \mathcal{L}_{SSL}(sa)$. Detailed configurations of the training loss and hyper-parameters can be found in the experimental Section VI.

3) Hyper-Parameter Learning: Hyper-parameter learning aims to determine the optimal configuration of hyper-parameters for a given machine learning task. Hyper-parameters are parameters that remain fixed during the training process of a machine learning model. In essence, the goal of hyper-parameter learning is to find a set of hyper-parameters that minimizes the loss or maximizes the accuracy of the objective learning task. Mathematically, it can be expressed as $\theta^* = \arg \min E_{(\mathcal{D}_{tr}, \mathcal{D}_{val}) \sim \mathcal{D}} L(g_\omega(\cdot), \theta, \mathcal{D}_{tr}, \mathcal{D}_{val})$, where L represents the objective function, $g_\omega(\cdot)$ denotes the learning algorithm applied to the hyper-parameters θ , and the model is trained on the training dataset \mathcal{D}_{tr} and validated on the validation dataset \mathcal{D}_{val} . Within our LwCL framework, the objective learner \mathcal{N}_θ^O aims to minimize the loss on the validation set $\mathcal{F}_{OL}^\omega(\theta, \omega; \mathcal{D}_{val})$ with respect to the hyper-parameters θ , which include parameters such as learning rate, batch size, optimizer, and loss weights. On the other hand, the constraint learner \mathcal{N}_ω^C is responsible for generating a learning algorithm by minimizing the training loss $\mathcal{F}_{CL}^\theta(\theta, \omega; \mathcal{D}_{tr})$ with respect to the model parameters ω , which encompass weights and biases.

C. TDC-Type Applications

As mentioned previously, TDC-type LwCL tasks, inspired by the concept of “divide and conquer” aim to analyze and formulate the coupling relationship. This approach involves decomposing the overall learning task into two distinct components: the objective learner \mathcal{N}_θ^O and the constraint learner \mathcal{N}_ω^C . In the subsequent sections, we delve into the practical

implementations of two notable application types, namely image deblurring and multi-task meta-learning learning and These applications serve as representative examples to showcase the efficacy and versatility of the the LwCL paradigm in addressing diverse learning challenges.

1) *Image Deblurring*: Image deblurring aims to recover a latent clear image \mathbf{u} from a blurred counterpart \mathbf{b} . The physical model governing this process is represented by $\mathbf{b} = \mathbf{K} * \mathbf{u} + \mathbf{n}$, where \mathbf{K} , \mathbf{n} , and $*$ denote the blur kernel, additional noise, and the two-dimensional convolution operator, respectively. Typically, image deblurring entails two main tasks: deconvolution, involving the estimation of sharp images from blurred observations, and denoising. Drawing inspiration from the plug-and-play framework, which leverages semi-quadratic splitting, the deblurring problem is decomposed into alternating iterations of two sub-problems concerning \mathbf{u} and an auxiliary variable \mathbf{z} . Within our LwCL framework, we define the constraint learner \mathcal{N}_ω^C as the fidelity learning sub-problem, addressing \mathbf{u} and \mathbf{z} . This can be formulated as $\{\mathbf{u}, \mathbf{z}\} = \arg \min_{\mathbf{u}, \mathbf{z}} \{\mathcal{F}_{\text{CL}}^\theta(\mathbf{u}, \mathbf{z}) := \|\mathbf{K} * \mathbf{u} - \mathbf{b}\|_2^2 + \mu \|\mathbf{u} - \mathbf{z}\|^2 + k \|\mathbf{W}\mathbf{u}\|_1\}$, where μ represents a penalty parameter, and \mathbf{W} denotes the wavelet transform matrix. The objective learner \mathcal{N}_θ^O can be viewed as the prior learning process, governed by a denoiser $\text{Net}_\theta(\mathbf{u})$, with regard to the variable θ . Mathematically, it can be expressed as $\theta = \arg \min_{\theta} \mathcal{F}_{\text{OL}}^\omega(\text{Net}_\theta(\mathbf{u}), \theta)$. For further details on the parameter configurations, please refer to Section VI.

2) *Multi-Task Meta-Learning*: Multi-task meta-learning represents a formidable challenge that revolves around swiftly adapting to novel tasks with limited examples. Among these tasks, meta-feature learning stands out as a prominent representative of multi-task and meta-learning, with the objective of acquiring a shared meta feature representation that encompasses all tasks. This is achieved by bifurcating the network architecture into two distinct components: the meta feature extraction part, responsible for generating the cross-task intermediate representation layers (parameterized by θ), and the task-specific part, characterized by the multinomial logistic regression layer (parameterized by ω^j). This framework allows for building accurate machine learning models utilizing a smaller training dataset, especially in the context of few-shot classification tasks, which are widely recognized in the field. Within the LwCL framework we propose, the intermediate representation layers that produce the meta-features can be viewed as the objective learner \mathcal{N}_θ^O for multiple task-specific assignments. Consequently, we optimize the performance of these meta-features using the validation set through the defined loss function $\mathcal{F}_{\text{OL}}^{\omega^j}(\theta; \mathcal{D}_{\text{val}}^j)$. Additionally, the forward propagation of the classification layers at the network's end serves as the constraint learner \mathcal{N}_ω^C , wherein the training set loss $\mathcal{F}_{\text{CL}}^\theta(\omega^j; \mathcal{D}_{\text{tr}}^j)$ is utilized to guide the learning process.

V. EXPERIMENTAL RESULTS

In this section, we first evaluate the learning mechanism of our proposed framework through a meticulous examination of numerical examples. This comprehensive evaluation will facilitate a profound understanding of the framework's underlying

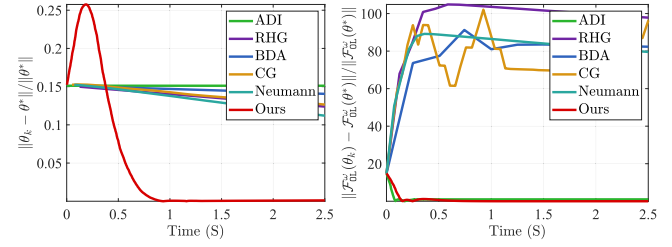


Fig. 2. Illustrating the convergence curve of $\|\theta_k - \theta^*\|/\|\theta^*\|$ and $\|\mathcal{F}_{\text{OL}}^\omega(\theta_k) - \mathcal{F}_{\text{OL}}^\omega(\theta^*)\|/\|\mathcal{F}_{\text{OL}}^\omega(\theta^*)\|$ among series of mainstream bi-level optimization strategies.

principles and intricacies of its learning processes. Subsequently, we proceed to conduct a series of rigorous and extensive experiments, aimed at meticulously scrutinizing the efficacy and viability of our proposed framework across a diverse array of learning paradigms and visual applications. All of these experiments are carried out on a high-performance computing system comprising an Intel Core i7-7700 CPU operating at a frequency of 3.6 GHz, 32 GB of RAM, and an NVIDIA GeForce RTX 2060 GPU with 6 GB of dedicated memory.

A. Mechanism Evaluation

First and foremost, we commence by assessing the convergence performance and computational complexity of our proposed algorithm on a numerical example. Specifically, we introduce a challenging toy example [39] wherein the CL problem is formulated as a non-convex optimization task:

$$\begin{aligned} & \min_{\theta \in \mathbb{R}, \omega \in \mathbb{R}^n} \|\theta - a\|^2 + \|\omega - a - c\|^2, \\ & \text{s.t. } [\omega]_i \in \underset{[\omega]_i \in \mathbb{R}}{\operatorname{argmin}} \sin(\theta + [\omega]_i - [c]_i), \forall i, \end{aligned} \quad (9)$$

where $[\omega]_i$ denotes the i -th component of ω , $a \in \mathbb{R}$ and $c \in \mathbb{R}^n$ denote adjustable parameters. For this particular numerical example, we set $a = 2$ and $[c]_i = 2$, for any $i = 1, 2, \dots, n$. The optimal solution for this numerical example is as follows

$$\theta = \frac{(1-n)a + nC}{1+n}, \text{ and } [\omega]_i = C + [c]_i - \theta, \forall i,$$

where $C = \operatorname{argmin}_C \{\|C - 2a\| : C = -\pi/2 + 2k\pi, k \in \mathbb{Z}\}$, and the optimal value is $(C - 2a)^2 - (C - 2a)^2/(1+n)$. To evaluate the convergence properties and computational complexity, we conducted two sets of experiments: one in low-dimensional simple scenarios with $n = 1$, and the other in high-dimensional scenarios with larger values of n .

In the case of one dimension, we initialize the point at $(\theta, \omega) = (3, 3)$ and the optimal solution is $(\theta^*, \omega^*) = (3/4\pi, 3/4\pi - 2)$. Fig. 2 compares the convergence curves of $\|\theta_k - \theta^*\|/\|\theta^*\|$ and $\|\mathcal{F}_{\text{OL}}^\omega(\theta_k) - \mathcal{F}_{\text{OL}}^\omega(\theta^*)\|/\|\mathcal{F}_{\text{OL}}^\omega(\theta^*)\|$ among series of mainstream bi-level optimization strategies, including Alternating Direction Iteration (ADI), CG [11], Neumann Series (NS) [12], RHG [5], and BDA [31]. It can be observed that these methods either deviate from the optimal solution throughout the iteration process or fail to achieve fast convergence. In contrast,

TABLE I

COMPARISON OF THE TIME COMPLEXITY (HOUR) AND SPACE COMPLEXITY (MB) ON HIGH-DIMENSIONAL NUMERICAL SCENARIOS UNDER A GIVEN CONVERGENCE CRITERION (I.E., $\|\theta_k - \theta_{k-1}\|/\|\theta_k\| \leq 10^{-5}$)

n	Metric	ADI	RHG	BDA	CG	NS	Ours
10^2	T	N/C	0.984	1.126	5.292	0.492	0.150
	M	N/C	9.961	10.552	2.032	1.983	0.065
10^3	T	N/C	18.829	18.688	92.420	9.286	1.428
	M	N/C	98.552	98.823	20.076	19.585	0.552
10^4	T	N/C	330.795	325.92	1957.161	193.13	14.346
	M	N/C	1004.681	1012.842	200.560	195.642	5.310
10^5	T	N/C	N/A	N/A	N/A	N/A	144.425
	M	N/C	N/A	N/A	N/A	N/A	53.030

Note that “N/A” means that the calculation time exceeds 1200 hours and the calculation memory exceeds 1024 MB. “N/C” indicates that the convergence criterion is not met. “T” and “M” represent “Time” and “Memory”, respectively. “ n ” denotes the dimension of ω . Scores ranked first and second are marked with bold and bold underline, respectively.

our proposed LwCL algorithm converges to the optimal solution more rapidly, showcasing its superiority.

To assess computational efficiency, we compare the time and space complexity between our algorithm and current mainstream algorithms in high-dimensional data scenarios. As depicted in Table I, due to the non-convex nature of the inner constrained objective function, ADI fails to converge in high-dimensional scenarios. Implicit gradient methods such as CG and Neumann exhibit lower computational complexity compared to explicit gradient methods like RHG and BDA, as they efficiently avoid the computationally expensive Hessian inverse. This renders them impractical for large-scale real-world scenarios, particularly when the dimensions of ω and θ are high. Conversely, our LwCL strategy surpasses these algorithms in terms of time consumption and memory footprint. As the dimensionality of the ω variable exponentially increases to $n = 10^5$, all algorithms except ours cause time and memory complexity to skyrocket, or even crash. This experiment theoretically validates our algorithm’s efficiency and applicability in high-dimensional scenarios compared to other approximation algorithms.

Furthermore, we conducted experiments on real-world datasets to validate the superiority of our learning strategy. We employed the LSGAN [40] as the foundational network architecture to validate the stability of our learning mechanism. Fig. 3 reports the score comparison of FID and JS in each training iteration of LSGAN on the CIFAR10 [41] and CIFAR100 [42]. The results clearly demonstrate that when combined with our LwCL framework, LSGAN exhibits enhanced training stability and achieves superior FID and Inception Score (IS) performance compared to directly applying alternating learning strategies.

B. AL-Type Applications

In the subsequent analysis, we explore four distinct applications, namely GAN and its variants, image generation, style transfer, and imitation learning, in order to validate the efficacy and versatility of our methodology. Importantly, we showcase that despite their diverse motivations and formulations, a wide

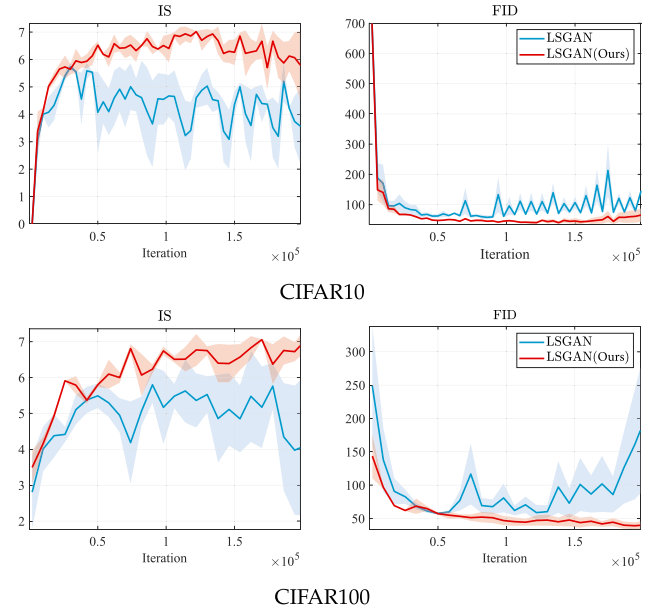


Fig. 3. Comparison of training efficiency results measured by FID and IS on CIFAR10 dataset (*listed top*) and CIFAR100 datasets (*listed bottom*). The shaded area represents the confidence interval, indicating uncertainty. More stable training convergence curves and better metric scores can be obtained by our LwCL framework.

range of AL-type LwCL applications, *ALL* can be uniformly improved by our flexible methodology.³

1) *GAN and Its Variants:* Initially, we conduct extensive experiments on synthesized datasets following a Mixed of Gaussian (MOG) distribution. These experiments aim to provide a quantitative and qualitative evaluation of our algorithm, considering aspects such as mode generation, computational efficiency, and training stability. To establish a performance comparison, we benchmark our approach against several state-of-the-art GAN architectures, including VGAN [1], WGAN [2], ProxGAN [16], and LCGAN [18]. For the synthetic data, we generate four distinct types of MOG distributions: 2D Ring (consisting of 5 or 8 2D Gaussians arranged in a ring), 2D Random (comprising 10 2D Gaussians with random magnitudes and positions), 2D Grid (comprising 25 2D Gaussians arranged in a grid), and 3D Cube (comprising 27 3D Gaussians within a cube). Each Gaussian distribution has a fixed variance of 0.02. During the training phase, we construct training batches with 512 samples from each mixture of Gaussian models, consisting of both real and generated data. Additionally, we sample 512 generated images for testing purposes.

To optimize the two networks, we uniformly employ the Adam optimizer, with a learning rate of 10^{-4} for the discriminator and 10^{-3} for the generator. Both the generator and discriminator adopt a 3-layer linear network with a width of 256. The activation function utilized is a leaky ReLU with a threshold of 0.2. To provide a comprehensive comparison, we employ three

³Due to mainstream bi-level optimization algorithms being unsuitable in high-dimensional real-world scenarios, we do not consider comparisons with these methods in the following large-scale applications.

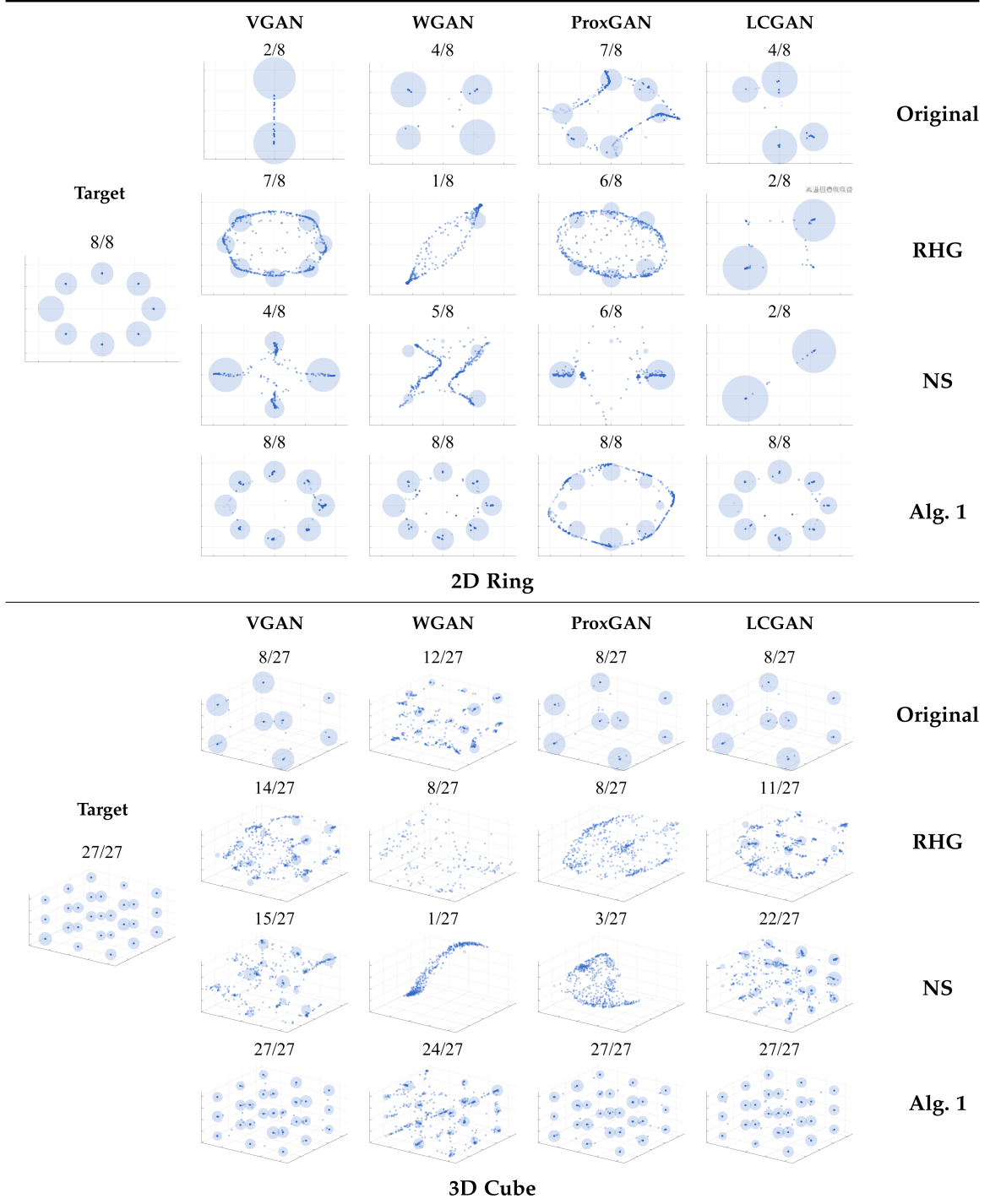


Fig. 4. Qualitative comparison among mainstream solution strategies under four GAN variants (i.e., VGAN, WGAN, ProxGAN, and LCGAN) as basic architectures, conducted on two synthetic MOG distribution datasets. The diversity of generated samples (number of generated classes/number of target classes) is listed at the top. The shading of the dots represents the density of the final distribution, with darker dots representing greater density.

well-established metrics: Frechet Inception Distance (FID) [44], Jensen-Shannon divergence (JS) [1], number of Modes (Mode). These metrics serve as a basis for evaluating and contrasting the performance of different approaches.

To demonstrate the superiority of our modeling and algorithm, Fig. 4 presents a comprehensive comparison of mainstream solution strategies in four GAN variants as basic architectures,

conducted on synthetic MOG datasets. We have chosen two exemplary first-order approximation approaches from Table I: RHG [5], a distinguished algorithm showcasing substantial performance advantages grounded in explicit gradient methodology, and NS [12], an algorithm highlighting notable efficiency gains through implicit gradient techniques. Across two types of MOG datasets (i.e., 2D Ring and 3D Cube), Fig. 4 presents a

TABLE II
COMPARISON RESULTS ON MAINSTREAM GANS (I.E., VGAN, LCGAN, WGAN, AND PROXGAN) WITH OR WITHOUT LwCL

Method	LwCL	2D Ring (max mode=8)			2D Random (max mode=10)		
		FID↓	JS↓	Mode↑	FID↓	JS↓	Mode↑
VGAN	✗	193.20 ± 65.30	0.63 ± 0.12	3.50 ± 1.00	77.58 ± 71.49	8.74 ± 0.02	3.75 ± 0.71
	✓	34.16 ± 10.23	0.40 ± 0.16	7.50 ± 1.00	23.29 ± 10.63	3.41 ± 0.07	7.75 ± 0.96
LCGAN	✗	15.01 ± 15.30	0.63 ± 0.12	3.50 ± 1.00	77.58 ± 11.49	0.71 ± 0.02	2.00 ± 0
	✓	1.19 ± 1.23	0.40 ± 0.16	7.50 ± 1.00	23.29 ± 0.63	0.33 ± 0.07	7.50 ± 0.71
WGAN	✗	0.42 ± 0.21	0.65 ± 0.13	6.25 ± 1.53	97.98 ± 0.10	0.75 ± 0	1.73 ± 1.63
	✓	0.16 ± 0.09	0.27 ± 0.25	7.00 ± 0.82	97.30 ± 1.49	0.70 ± 0.06	7.33 ± 0.81
ProxGAN	✗	15.01 ± 15.30	0.63 ± 0.12	3.50 ± 1.00	74.05 ± 8.77	0.75 ± 0.17	3.50 ± 1.91
	✓	8.82 ± 17.25	0.58 ± 0.26	6.50 ± 3.00	20.44 ± 11.28	0.36 ± 0.01	7.50 ± 0.71
Method	LwCL	2D Grid (max mode=25)			3D Cube (max mode=27)		
		FID↓	JS↓	Mode↑	FID↓	JS↓	Mode↑
VGAN	✗	10.14 ± 1.36	0.79 ± 0.24	12.50 ± 1.00	12.28 ± 26.10	0.48 ± 0.08	8.50 ± 1.00
	✓	0.81 ± 0.24	0.62 ± 0.13	18.5 ± 1.00	0.528 ± 0.16	0.61 ± 0.30	23.00 ± 1.40
LCGAN	✗	50.73 ± 47.08	0.64 ± 0.21	11.50 ± 8.1	68.80 ± 60.85	0.87 ± 0.17	6.00 ± 3.16
	✓	0.42 ± 0.13	0.62 ± 0.27	17.25 ± 7.27	30.5 ± 45.81	0.70 ± 0.30	17.33 ± 14.15
WGAN	✗	171.31 ± 77.46	0.89 ± 0.29	5.00 ± 1.30	12.00 ± 0.90	0.62 ± 0.07	15.00 ± 0.41
	✓	15.91 ± 1.43	0.68 ± 0.14	18.50 ± 0.58	0.80 ± 0.20	0.21 ± 0.03	24.00 ± 0.51
ProxGAN	✗	38.29 ± 47.08	0.67 ± 0.21	11.5 ± 8.10	111.64 ± 63.96	0.85 ± 0.03	3.67 ± 2.89
	✓	0.46 ± 0.24	0.60 ± 0.23	18.25 ± 7.63	52.10 ± 86.98	0.69 ± 0.30	17.67 ± 14.47

We report the average FID↓, JS↓ and Mode↑ scores on four MOG synthesized datasets, i.e., 2D Ring, 2D Rand, 2D Grid and 3D Cube. The score represents the mean and standard deviation of the results from five trials. Note that scores ranked first and second are marked with bold and bold underline, respectively.

comprehensive comparison of the sample quantities generated by 4 distinct approximation algorithms within 4 sophisticated GAN variant frameworks. Columns 2 to 5 distinctly portray outcomes derived by applying diverse solving algorithms within the specified structure of the GAN. It is evident that the original models struggle to capture a significant number of distributions, leading to severe mode collapse and unsatisfactory performance. Additionally, under the solution of two types of approximation algorithms, various GAN models also struggle to capture the complete sample distribution, resulting in suboptimal generation outcomes. In contrast, our method outperforms by yielding a sample distribution that aligns more closely with the target distribution, as indicated by the quantity of generated samples.

Table II further demonstrates the effectiveness of our methodology in alleviating the mode collapse issue. Specifically, WGAN combined with LwCL achieves the lowest FID score in the 2D Ring distribution, and obtains the lowest JS score in the 3D Cube dataset. It is noteworthy that our flexible LwCL methodology uniformly improves a wide range of existing GANs, enhancing their overall performance.

2) *Image Generation*: In our experimental evaluation, we examine the performance of several well-established generative models, namely DCGAN [17], LSGAN [40], and SNGAN [45]. To assess their capabilities, we employ widely used benchmark datasets, including CIFAR10 [41], CIFAR100 [42] and CelebA-HQ [43]. For evaluating the generative models, we employ two widely recognized metrics: Inception Score (IS) for evaluating generation quality and diversity, and Fréchet Inception Distance (FID) for capturing the issue of mode collapse. Under our LwCL framework, we consider DCGAN, which incorporates standard binary cross-entropy loss for unsupervised training and employs a coupled game process of OL and CL. The objective functions $\mathcal{F}_{\text{OL}}^{\omega}$ and $\mathcal{F}_{\text{CL}}^{\theta}$ for DCGAN are

TABLE III
COMPARISON RESULTS OF FID AND IS SCORE ON CIFAR10 AND CIFAR100 DATASET

Method	LwCL	CIFAR10		CIFAR100	
		IS↑	FID↓	IS↑	FID↓
DCGAN	✗	6.63	49.03	6.56	57.37
	✓	7.06	42.23	6.87	44.18
LSGAN	✗	5.57	66.68	3.81	145.54
	✓	7.54	32.50	7.30	35.72
SNGAN	✗	7.48	26.51	7.99	25.33
	✓	7.58	22.81	8.27	21.37

Note that scores ranked first and second are marked with bold and bold underline, respectively.

defined as follows: $\mathcal{F}_{\text{OL}}^{\omega} := E_{\mathbf{v} \sim \mathcal{N}(0,1)} [\log(1 - D(G(\mathbf{v})))]$, and $\mathcal{F}_{\text{CL}}^{\theta} := E_{\mathbf{u} \sim P_{\text{data}}} [\log(D(\mathbf{u}))] + E_{\mathbf{v} \sim \mathcal{N}(0,1)} [\log(1 - D(G(\mathbf{v})))]$. Similarly, for LSGAN, which employs a least squares loss, the objective functions $\mathcal{F}_{\text{OL}}^{\omega}$ and $\mathcal{F}_{\text{CL}}^{\theta}$ are constructed as follows: $\mathcal{F}_{\text{OL}}^{\omega} := E_{\mathbf{v} \sim \mathcal{N}(0,1)} [D(G(\mathbf{v})) - c]^2$, and $\mathcal{F}_{\text{CL}}^{\theta} := E_{\mathbf{u} \sim P_{\text{data}}} [D(\mathbf{u}) - b]^2 + E_{\mathbf{v} \sim \mathcal{N}(0,1)} [D(G(\mathbf{v})) - a]^2$. As for SNGAN, it incorporates spectral normalization to ensure the 1-Lipschitz continuity constraint. The objective function $\mathcal{F}_{\text{CL}}^{\theta}$ for SNGAN is defined as follows: $\mathcal{F}_{\text{CL}}^{\theta} := \sup_{\|D\| \leq 1} E_{\mathbf{u} \sim P_{\text{data}}} [D(\mathbf{u})] - E_{\mathbf{v} \sim \mathcal{N}(0,1)} [D(G(\mathbf{v}))]$. Furthermore, in our face generation experiment on the high-resolution CelebA-HQ dataset [43], we employ StyleGAN as the backbone architecture.

Table III further highlights the consistent performance improvements achieved by state-of-the-art GAN architectures when incorporated into our LwCL framework. Moreover, Fig. 5 visually demonstrates the efficacy of our LwCL methodology in conjunction with StyleGAN. It showcases the superior style-content trade-off achieved, validating the versatility and



Fig. 5. Comparison results of face generation on CelebA-HQ dataset [43]. Given the same latent feature variables, our method (i.e., StyleGAN with LwCL) is capable of generating more natural and realistic face details, with sharper and well visualized facial contours.

effectiveness of our flexible solution strategy. Notably, our approach excels in generating realistic facial structures while effectively mitigating twist distortion.

3) *Style Transfer*: We select the CycleGAN model [9] as the foundation for our architecture and conduct experiments on the FFHQ dataset [46] to explore unsupervised style transfer. Our approach leverages two Generator networks and two Discriminator networks, forming a bidirectional LwCL framework. This framework incorporates cycle-consistency loss in two loops to assess the ability to reconstruct an image from its transformed counterpart. The cycle consistency loss, denoted as $\mathcal{L}_{cyc}(G_1, G_2)$, captures the discrepancy between the original image and its reconstructed version in both the forward and backward mapping processes. Mathematically, it is defined as the summation of the ℓ_1 norm of the difference between the transformed and reconstructed images, computed as $\mathcal{L}_{cyc}(G_1, G_2) = E_{\mathbf{x} \sim P_{\text{data}}(\mathbf{x})}[\|G_2(G_1(\mathbf{x}))\|_1] + E_{\mathbf{y} \sim P_{\text{data}}(\mathbf{y})}[\|G_1(G_2(\mathbf{y}))\|_1]$. In the bidirectional mapping process, the optimization of variables in the two objective functions can be mutually exchanged and modeled. We ensure a fair comparison by following the experimental setups and model architecture detailed in [9].

Fig. 6 visually demonstrates the remarkable advantages of our proposed framework in generating samples of higher quality and richer detailed textures. In comparison to the sparse and unrealistic textures produced by the standard CycleGAN, it is evident that the network integrated with our LwCL framework can generate zebra stripes that are more abundant, natural, and realistic. In Fig. 7, we observe significant fluctuations in the visual perceptual quality of the generated images by the standard CycleGAN throughout the training process. With the standard CycleGAN, high-quality zebra images can be generated at 40 epochs. However, at 60 epochs, a small amount of background stripes starts to appear, and by 120 epochs, the stripes that should be generated on the horse are completely transferred to the background. In contrast, when our LwCL strategy is incorporated, the generation of zebra patterns becomes gradually stable, and the authenticity of the texture is significantly enhanced. This improvement effectively mitigates the occurrence of mode collapse, ensuring the preservation of desirable characteristics in the generated images.

4) *Imitation Learning*: In the formulated Markov decision process, denoted as $\mathcal{M} = (\mathcal{S}, \mathcal{A}, \rho, P, \mathcal{R}, \gamma)$, we define the



Fig. 6. Comparison results for style transfer (i.e., horse → zebra) on FFHQ [46]. CycleGAN combining with our proposed LwCL methodology could generate more accurate transformation full of realistic textures.

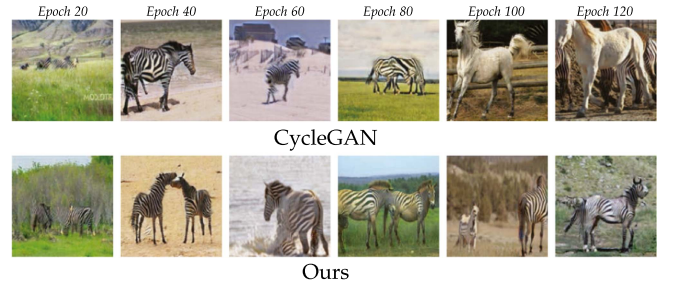


Fig. 7. Visualization comparison during training between standard CycleGAN and our method. It can be observed that standard CycleGAN is not stable (with or without streaks), while the generation quality after introducing LwCL is significantly improved.

action space \mathcal{A} , state space \mathcal{S} , and reward function $\mathcal{R} : \mathcal{S} \times \mathcal{A} \mapsto \mathbb{R}$. The initial state s_0 is drawn from the distribution $\rho(\cdot)$, and the discount factor $\gamma \in (0, 1)$ is applied. In this context, the actor π interacts with the environment to learn the state-action value function $Q^\pi(s, a)$, followed by the update of the

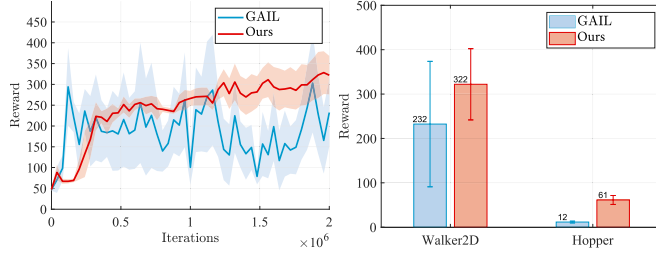


Fig. 8. Comparison of reward scores in terms of the training curve (*left*), and final quantitative performance under two simulated environments, i.e., “Walker2D” and “Hopper” (*right*). The shaded area represents the confidence interval, indicating uncertainty.

actor π based on $Q^\pi(s, a)$. The objective of the policy is to maximize the expected discounted cumulative reward, given by: $\pi^* = \arg \max_\pi \mathbb{E}_{s_0 \sim p_0, a_0 \sim \pi}(Q^\pi(s_0, a_0))$, where s_0 , a_0 , and p_0 represent the initial state, initial action, and initial state distribution, respectively. For our experiment, we employ the PyBullet physics simulator and publicly available datasets tailored for data-driven deep reinforcement learning. Following the definitions and experimental settings of recent studies [20], [21], we design an agent with an actor-critic structure to predict actions that deceive the discriminator. The discriminator, on the other hand, is trained to distinguish between samples generated by the policy π^* and an expert policy $\hat{\pi}$. To compute the reward function \mathcal{R} , we adopt the form $h(s, a) = \log(D(s, a)) - \log(1 - D(s, a))$. Additionally, both Generative Adversarial Imitation learning (GAIL) and our method incorporate the R_1 gradient penalty regularizers.

Fig. 8 presents the average policy return and standard error for two simulated environments, namely “Walker2D” and “Hopper”. The average policy return and its standard error are plotted to illustrate the performance of GAIL. It is evident that the GAIL curve exhibits significant instability and lacks a convergent trend. In contrast, our proposed solution technique ensures a more stable convergence during training with reduced deviation. Additionally, we provide the final return achieved throughout the training episodes, which serves as an indicator of the performance improvement achieved by GAIL when employing our novel solution techniques.

C. ART-Type Applications

In the subsequent sections, we delve into three distinct applications, each accompanied by the introduction of relevant task constraints. These applications encompass medical image analysis, low-light image enhancement, and hyper-parameter learning.

1) Medical Image Analysis: We evaluate the segmentation performance on a hybrid dataset by using 426 mixed medical scans, which is sampled from three standard datasets, ABIDE, ADNI and PPMI. During the training phase, the scanned images are divided into 346, 40, and 40 volumes for training, validation, and testing, respectively. To capture both global and local differences in appearance, we define the energy function $\mathcal{L}_{reg} = \mathcal{L}_{sim} + \lambda_{scc} * \mathcal{L}_{scc}$, where \mathcal{L}_{sim}

TABLE IV
COMPARISON RESULTS OF DIFFERENT METHODS FOR JOINT REGISTRATION AND SEGMENTATION TASKS

Method	Dice↑	HD95↓	ASD↓
Medical Image Registration			
Initial	64.5 ± 6.0	2.99 ± 0.79	0.55 ± 0.15
VxM	76.8 ± 1.5	2.39 ± 0.51	0.43 ± 0.09
LKU-Net	77.2 ± 1.5	2.28 ± 0.47	0.41 ± 0.09
TransMorph	77.9 ± 1.3	2.40 ± 0.48	0.42 ± 0.09
SST	74.2 ± 2.6	2.89 ± 0.58	0.51 ± 0.12
DeepAtlas	76.9 ± 2.1	2.58 ± 0.57	0.46 ± 0.13
DataAug	78.1 ± 1.9	2.34 ± 0.54	0.40 ± 0.11
BRBS	80.1 ± 1.9	2.35 ± 0.53	0.42 ± 0.13
Ours	80.3 ± 1.4	2.23 ± 0.49	0.39 ± 0.10
Medical Image Segmentation			
UNet	58.1 ± 7.5	12.8 ± 3.23	2.47 ± 0.98
MASSL	66.2 ± 4.5	10.7 ± 2.95	1.79 ± 0.57
CPS	73.1 ± 4.2	3.66 ± 1.34	0.67 ± 0.19
SST	76.5 ± 2.2	2.93 ± 0.72	0.55 ± 0.18
DeepAtlas	77.8 ± 1.7	2.89 ± 0.62	0.53 ± 0.15
DataAug	78.9 ± 3.0	2.97 ± 0.46	0.56 ± 0.16
BRBS	82.3 ± 1.8	2.84 ± 0.59	0.50 ± 0.19
Ours	83.4 ± 1.3	2.55 ± 0.54	0.43 ± 0.15

Note that scores ranked first and second are marked with bold and bold underline, respectively.

is the multi-scale local cross-correlation in appearance [27], and \mathcal{L}_{scc} is the semantic content consistency loss [24], i.e., $\mathcal{L}_{scc} = \frac{1}{2}(\text{KL}(p_t || \frac{p_w + p_t}{2}) + \text{KL}(p_w || \frac{p_w + p_t}{2}))$. Here KL denotes the Kullback-Leibler divergence, and p_w and p_t are the warped prediction and target prediction, respectively. For segmentation, the energy function is formulated as a composite loss, denoted as $\mathcal{L}_{seg} = \mathcal{L}_{dice} + \lambda_{mce} * \mathcal{L}_{mce}$. This hybrid loss integrates the multi-class cross entropy loss \mathcal{L}_{mce} with the dice coefficient loss \mathcal{L}_{dice} , establishing a balanced and robust framework for segmentation tasks [25]. In our training, we empirically set the balancing parameters $\lambda_{scc} = 10$ and $\lambda_{mce} = 1$, and use ADAM optimizer with learning rate of $4 * 10^{-4}$. To evaluate the performance of registration and segmentation, we employed well-established metrics such as the Dice score, Hausdorff distance (HD95), and average surface distance (ASD). We compare our method to several state-of-the-art methods, including a) Deep learning registration-based segmentation methods, VxM [47], LKU-Net [48], and TransMorph [49]. b) Deep learning segmentation methods, UNet [7], MASSL [50], and CPS [51]. d) joint registration and segmentation methods, SST [26], DeepAtlas [24], DataAug [27], and BRBS [25].

Table IV presents quantitative comparisons for joint registration and segmentation tasks, demonstrating that our method achieved the highest Dice score and the lowest HD95 and ASD metrics in registration and segmentation, respectively. Fig. 9 presents the 2D visualization results of the registration method compared to other approaches. Traditional registration methods or approaches that simply separate the two tasks have shown more registration errors, as indicated by the increased number of error points within the red box. In contrast, our method demonstrates the smallest mislabeling regions on the lateral

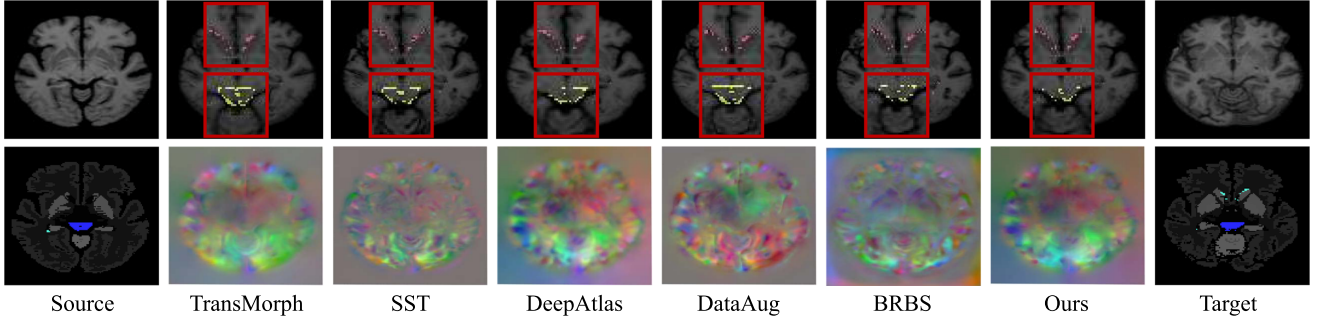


Fig. 9. Visual results of state-of-the-art medical image registration methods for the lateral ventricle (LV) and brain stem (BS) with 2D visualization. The upper row displays the error map between the warped label and the target, highlighted in shades of pink and yellow. The lower row illustrates the deformable field, along with the labels for both the source and the target.

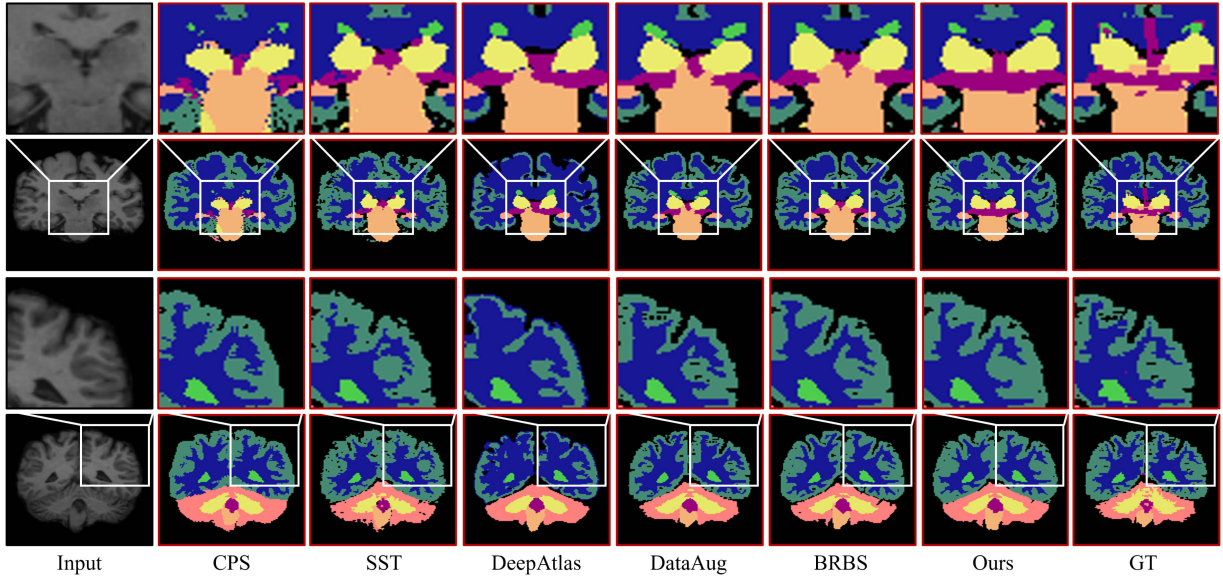


Fig. 10. Qualitative evaluation of various medical image segmentation methods for the brain anatomical structures, with 2D slice visualization *Top*: small brain structure 3rd/4th Ventricle (Ven); *Bottom*: large brain structure Cerebral White Matter (CrWM).

ventricle (LV) and brainstem (BS), as indicated by the yellow and pink areas. Additionally, we provide qualitative results in Fig. 10, illustrating the robust segmentation performance of our method at complex termination sites in the structural white matter of the brain and the finer segmentation quality achieved on the cerebellar tissue and the 3/4 ventricles.

2) *Low-Light Image Enhancement*: We conduct low-light enhancement experiments on DarkFace dataset, and adopt the well-known no reference metrics (i.e., DE and LOE). To benchmark our method, we compare it against several state-of-the-art approaches, including RetinexNet [52], KinD [53], ZeroDCE [54], DeepUPE [55], FIDE [56], DRBN [57] and SCI [37]. As mentioned in [37], we introduce the pixel fidelity term \mathcal{L}_p and a smoothness term \mathcal{L}_s for \mathcal{N}_θ^O , which are formulated as $\mathcal{L}_p = \sum_{t=1}^T \|\mathbf{x}^t - \hat{\mathbf{y}}_{t-1}\|$, $\mathcal{L}_s = \sum_{i=1}^N \sum_{j \in \mathcal{N}(i)} w_{i,j} \|\mathbf{x}_i^t - \mathbf{x}_j^t\|$, where $\hat{\mathbf{y}}_{t-1}$ denotes the self-calibrated variable, N is the total number of pixels, $w_{i,j}$ represents the weight function. As for \mathcal{N}_ω^C , we also introduce

the anchor-based multi-task loss and progressive anchor loss [38], defined as: $\mathcal{F}_{CL}^\theta := \mathcal{L}_{SSL}(a) + \lambda \mathcal{L}_{SSL}(sa)$. Here, $\mathcal{L}_{SSL}(p_i, p_i^*, t_i, g_i, a_i) = \frac{1}{N_{conf}} ((\sum_i L_{conf}(p_i, p_i^*)) + \frac{\beta}{N_{loc}} \sum_i p_i^* L_{loc}(t_i, g_i, a_i))$, where N_{conf} and N_{loc} indicate the number of positive and negative anchors, and the number of positive anchors, respectively. L_{loc} is the smooth loss between the predicted box t_i and ground-truth box g_i using the anchor a_i , and L_{conf} is the softmax loss in terms of two classes.

In Fig. 11, we compare the visualization results. It can be seen that although some methods can successfully enhance the brightness of the image, none of them can restore the clear image texture. The DE score is reported below, and a higher DE value indicates better visual quality. In comparison, our method produces the most visually pleasing results, can not only learn to enhance the dark area while restoring more visible details but also avoids over-exposure artifacts. We report the quantitative results in Table V. It can be seen that our method numerically outperforms existing methods by large margins and ranks first



Fig. 11. Visual results of state-of-the-art low-light enhancement methods on the Darkface dataset. Our method improves brightness for a more natural and realistic effect. Larger DE indicates more perceptually favored quality. Zoom-in regions are used to illustrate the visual differences.

TABLE V
QUANTITATIVE RESULTS (DE \uparrow , LOE \downarrow) ON THE DARKFACE DATASET

Metric	RetinexNet	DeepUPE	KinD	ZeroDCE
DE \uparrow	7.125	7.089	7.053	7.150
LOE \downarrow	555.990	144.242	277.523	142.544
Metric	FIDE	DRBN	SCI	Ours
DE \uparrow	6.106	7.187	7.005	7.254
LOE \downarrow	280.616	495.748	84.745	78.976

Note that scores ranked first and second are marked with bold and bold underline, respectively.

TABLE VI
REPORTING RESULTS OF EXISTING METHODS FOR SOLVING DATA HYPER-CLEANING TASKS

Method	MNIST		FashionMNIST		CIFAR10	
	F1 score	Time (s)	F1 score	Time (s)	F1 score	Time (s)
CG	85.96	0.1799	85.13	0.2041	69.10	0.4796
Neumann	87.54	0.1723	87.28	0.1958	68.87	0.4694
RHG	89.36	0.4131	87.12	0.4589	68.27	1.3374
T-RHG	89.77	0.2623	86.76	0.2840	68.06	0.8409
BDA	90.38	0.6694	88.24	0.8571	67.33	1.4869
Ours	91.41	0.0279	90.03	0.0289	70.10	0.0797

F1 score denotes the harmonic mean of the precision and recall. Note that scores ranked first and second are marked with bold and bold underline, respectively.

across all metrics. This further endorses the superiority of our method over current state-of-the-art methods in generating high-quality visual results.

3) *Hyper-Parameter Learning*: We consider a specific data hyper-cleaning example [58]. In this scenario, we aim to train a linear classifier using a given image dataset, but encounter the issue of corrupted training labels. To address this, we adopt softmax regression with parameters ω as our classifier and introduce hyperparameters θ to assign weights to the training samples. Initially, we define the cross-entropy function $\ell(\omega; \mathbf{u}_i, \mathbf{v}_i)$ which measures the classification loss using the classification parameter ω and the data pairs $(\mathbf{u}_i, \mathbf{v}_i)$. The training and validation sets are denoted as \mathcal{D}_{tr} and \mathcal{D}_{val} , respectively. Next, we introduce the CL function $\mathcal{F}_{\text{CL}}^{\theta}$ as the following weighted training loss, given by $\mathcal{F}_{\text{CL}}^{\theta}(\omega) = \sum_{((u)_i, (v)_i) \in \mathcal{D}_{\text{tr}}} [\delta(\theta)]_i \ell(\omega; \mathbf{u}_i, \mathbf{v}_i)$. Here θ represents the hyperparameter vector that penalizes the objective for different training samples. The element-wise sigmoid function $\delta(\theta)$ is applied to restrict the weights within the range of $[0, 1]$. Furthermore, we define \mathcal{F}_{OL} as the cross-entropy loss with ℓ_2 regularization on the validation set, i.e., $\mathcal{F}_{\text{OL}}(\theta) = \sum_{((u)_i, (v)_i) \in \mathcal{D}_{\text{val}}} \ell(\omega(\theta); \mathbf{u}_i, \mathbf{v}_i) + \eta \|\omega(\theta)\|^2$, where η is the trade-off parameter. Three well known datasets including MNIST, FashionMNIST and CIFAR10 are used to conduct the experiments. Specifically, the training, validation and test sets consist of 5000, 5000, 10000 class-balanced samples randomly selected to construct \mathcal{D}_{tr} , \mathcal{D}_{val} and $\mathcal{D}_{\text{test}}$, then half of the labels in \mathcal{D}_{tr} are tampered. We adopted the architectures proposed by [5] as the feature extractor for all the compared methods.

Table VI presents a comprehensive comparison of our LwCL framework with popular first-order bi-level optimization algorithms, including explicit gradient approximation algorithms: RHG [5], Truncated RHG (T-RHG) [6], and BDA [31]; as well as implicit gradient approximation algorithms: CG [11], Neumann [12], in terms of F1 score and running time. The results clearly demonstrate the superior performance of our method in terms of F1 score compared to the other hyperparameter optimization techniques. Notably, our method significantly outperforms all relevant algorithms in terms of running time, achieving a substantial improvement of nearly an order of magnitude. This further endorses the superiority of our flexible solution strategy over current mainstream optimization algorithms, validating the low complexity and high efficiency.

D. TDC-Type Applications

In the subsequent sections, we proceed to showcase the efficacy of LwCL through the evaluation of its performance in two prominent TDC-type LwCL applications: image deblurring and multi-task meta-learning.

1) *Image Deblurring*: We conduct image deblurring experiment on a data benchmark, containing 400 images from the Berkeley Segmentation dataset, 4744 images from the Waterloo Exploration database, 900 images from the DIV2K dataset and 2750 images from the Flickr2K dataset. More specifically, we used the DRUNet in DPIR [8] containing four scales as the base network. In the specific implementation, the subproblem for \mathbf{u} is solved by closed-form solution based on the fast Fourier

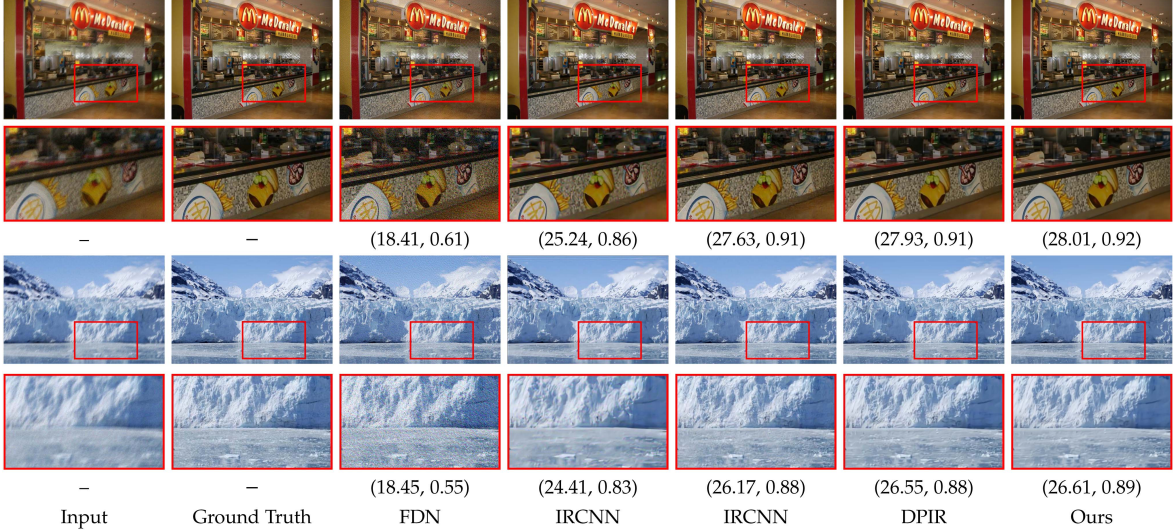


Fig. 12. Visual results of state-of-the-art image deblurring methods. Our method maintains a more realistic, natural and clear restoration result in terms of tone and texture. Two well-known metrics (PSNR↑, SSIM↑) are listed to quantify the generated image quality.

TABLE VII
COMPARISON OF QUANTITATIVE RESULTS (I.E., AVERAGED PSNR AND SSIM SCORES) AMONG STATE-OF-THE-ART IMAGE DEBLURRING METHODS (I.E., FDN [59], IRCNN [32], IRCNN+ and DPIR [8])

Blur Kernel	Metric	Method				
		FDN	IRCNN	IRCNN+	DPIR	Ours
K_1	PSNR	18.741	26.281	27.761	28.168	28.236
	SSIM	0.472	0.876	0.880	0.889	0.890
K_2	PSNR	17.977	27.361	27.532	28.066	28.132
	SSIM	0.437	0.881	0.874	0.887	0.888
K_3	PSNR	17.775	28.364	27.586	28.295	28.364
	SSIM	0.431	0.895	0.868	0.890	0.891
K_4	PSNR	17.905	25.291	27.400	27.918	27.970
	SSIM	0.435	0.858	0.872	0.884	0.885
K_5	PSNR	18.273	27.642	27.640	28.450	28.471
	SSIM	0.436	0.879	0.866	0.888	0.888

The default noise intensity n is set to 7.65. The quality scores of the various methods are compared under different sizes of blur kernels K_i , $i = 1, \dots, 5$. Note that scores ranked first and second are marked with bold and bold underline, respectively.

transform, and the subproblem on \mathbf{z} is obtained by an updated denoiser $\text{Net}_\theta(\mathbf{u})$. Unlike the original method that treats the denoiser as a fixed pre-trained network, under our LwCL framework, the parameters of the deblurring network are dynamically updated as learnable variables. As discussed earlier, it can be understood that the lower variable ω is a combination about two optimized variables, i.e., $\omega = \{\mathbf{u}, \mathbf{z}\}$. Thus, by jointly learning two sub-tasks, our method can improve robustness and generalization to various complex noise scenarios. Each scale has a skip connection between the 2×2 stride convolution downscale and the 2×2 transpose convolution upscale operations. The number of channels per layer from the first to fourth scale is 64, 128, 256 and 512 respectively. Four blocks of residuals are used in the down-sampling and up-sampling operations at each scale.

We qualitatively and quantitatively evaluated the performance of a series of relevant methods, including FDN [59],

IRCNN [32], IRCNN+ and DPIR [8]). As shown in Table VII, we report the performance of the current methods under five different sizes of blur kernel settings (i.e., K_i , $i = 1, \dots, 5$). All experiments were performed under a uniform noise criterion with a default noise level $n = 7.65$. In comparison, our method achieves the best PSNR scores under all five blurs and performs best in both average PSNR and SSIM scores. In addition, we show a visualization of the perceptual results in Fig. 12. As can be seen, for the deblurring task, our method outperforms other methods in terms of color recovery, detail retention, and achieves the best visual performance. This further endorses the superiority of our method over current state-of-the-art methods in image deblurring.

2) *Multi-Task Meta-Learning*: We conduct the N -way M -shot classification experiments where each task is to discriminate N separate classes and it is to learn the hyper-parameter θ such that each task can be solved only with M training samples. Typically, we separate the network architecture into two parts: the cross-task intermediate representation layers (parameterized by θ) outputs the meta features and the multinomial logistic regression layer (parameterized by ω^j) as our ground classifier for the j -th task. During training, we conduct our experiment on a meta training data set $\mathcal{D} = \{\mathcal{D}^j\}$, where $\mathcal{D}^j = \mathcal{D}_{\text{tr}}^j \cup \mathcal{D}_{\text{val}}^j$ is linked to the j -th task. Then, we consider the cross-entropy function $\ell(\theta, \omega^j; \mathcal{D}_{\text{tr}})$ as the task-specific loss for the j -th task and thus the $\mathcal{F}_{\text{CL}}^\theta$ can be defined as $\mathcal{F}_{\text{CL}}^\theta(\{\omega^j\}) = \sum_j \ell(\theta, \omega^j; \mathcal{D}_{\text{tr}}^j)$. Similarly, we also utilize the cross-entropy function but define it based on $\mathcal{D}_{\text{val}}^j$ as $\mathcal{F}_{\text{OL}}^{\{\omega^j\}}(\theta) = \sum_j \ell(\theta, \omega^j; \mathcal{D}_{\text{val}}^j)$. We validate the performance based on the widely used Omniglot dataset, and consider ResNet-12 with Residual blocks as the backbone. Besides, we introduce the task-and-layer-wise attenuation [60] to control the influence of prior knowledge for each task and layer.

As illustrated in Table VIII, we conducted a series of N -way M -shot classification experiments. We compare our algorithm with several advanced approximation algorithms, such as MAML [3], Meta-SGD [33], Reptile [34], iMAML [4],

TABLE VIII

MEAN TEST ACCURACY OF VARIOUS METHODS (MODEL-BASED METHODS AND GRADIENT-BASED BI-LEVEL METHODS) ON FEW-SHOT CLASSIFICATION CLASSIFICATION PROBLEMS (1-SHOT AND 5-SHOT, I.E., $M = 1, 5, N = 5, 20, 30, 40$) ON OMNIGLOT

Method	5-way		20-way		30-way		40-way	
	1-shot	5-shot	1-shot	5-shot	1-shot	5-shot	1-shot	5-shot
MAML	98.70 ± 0.40%	99.91 ± 0.10%	95.80 ± 0.30%	98.90 ± 0.20%	86.86 ± 0.49%	96.86 ± 0.19%	85.98 ± 0.45%	94.46 ± 0.13%
Meta-SGD	97.97 ± 0.70%	98.96 ± 0.20%	93.98 ± 0.43%	98.42 ± 0.11%	89.91 ± 0.04%	96.21 ± 0.15%	87.39 ± 0.43%	95.10 ± 0.15%
Reptile	97.68 ± 0.04%	99.48 ± 0.06%	89.43 ± 0.14%	97.12 ± 0.32%	85.40 ± 0.30%	95.28 ± 0.30%	82.50 ± 0.30%	92.79 ± 0.33%
iMAML	99.16 ± 0.35%	99.67 ± 0.12%	94.46 ± 0.42%	98.69 ± 0.10%	89.52 ± 0.20%	96.51 ± 0.08%	87.28 ± 0.21%	95.27 ± 0.08%
RHG	98.64 ± 0.21%	99.58 ± 0.12%	96.13 ± 0.02%	99.09 ± 0.08%	93.92 ± 0.18%	98.43 ± 0.08%	90.78 ± 0.20%	96.79 ± 0.10%
T-RHG	98.74 ± 0.21%	99.71 ± 0.07%	95.82 ± 0.20%	98.95 ± 0.07%	94.02 ± 0.18%	98.39 ± 0.07%	90.73 ± 0.20%	96.79 ± 0.10%
Ours	99.67 ± 0.05%	99.67 ± 0.06%	96.33 ± 0.21%	99.07 ± 0.11%	95.53 ± 0.25%	98.50 ± 0.14%	91.21 ± 0.28%	97.33 ± 0.16%

We use \pm to represent 95% confidence intervals over tasks. Note that scores ranked first and second are marked with bold and bold underline, respectively.

RHG [5], and T-RHG [6]. In comparison, our algorithm achieved the highest classification accuracy except in the 5-way 5-shot and 20-way 5-shot tasks. Indeed, with more complex few-shot classification problems (such as 30-way and 40-way), our LwCL showed significant advantages over other methods. This further illustrates the versatility and effectiveness of our algorithm in the field of complex learning.

VI. CONCLUSIONS AND FUTURE WORKS

In this work, we have introduced a novel perspective called Learning with Constraint Learning (LwCL) to provide a deeper understanding of their underlying coupling mechanisms for efficiently solving contemporary complex problems in machine learning and computer vision. Our proposed framework provides a unified understanding of the intrinsic mechanisms behind diverse problems. By establishing a general hierarchical optimization framework and a dynamic best response-based fast solution strategy, we have demonstrated the effectiveness of our approach in formulating and addressing LwCLs. Through extensive experiments we have verified the efficiency of our proposed framework in solving a wide range of LwCL problems, spanning three categories and nine different types. Future research can focus on further exploring and extending the capabilities of LwCL in addressing even more challenging problems and advancing the state-of-the-art in machine learning and computer vision. The findings presented in this paper contribute to a deeper understanding and efficient resolution of complex problems in learning and vision, providing valuable insights for future research and applications in the field.

REFERENCES

- [1] I. Goodfellow et al., “Generative adversarial nets,” *Adv. Neural Inf. Process. Syst.*, vol. 27, pp. 2672–2680, 2014.
- [2] M. Arjovsky, S. Chintala, and L. Bottou, “Wasserstein generative adversarial networks,” in *Proc. Int. Conf. Mach. Learn.*, 2017, pp. 214–223.
- [3] L. Collins, A. Mokhtari, and S. Shakkottai, “Task-robust model-agnostic meta-learning,” in *Proc. Int. Conf. Neural Inf. Process. Syst.*, 2020, pp. 18860–18871.
- [4] A. Rajeswaran, C. Finn, S. M. Kakade, and S. Levine, “Meta-learning with implicit gradients,” in *Proc. Int. Conf. Neural Inf. Process. Syst.*, 2019, pp. 113–124.
- [5] L. Franceschi, M. Donini, P. Frasconi, and M. Pontil, “Forward and reverse gradient-based hyperparameter optimization,” in *Proc. Int. Conf. Mach. Learn.*, PMLR, 2017, pp. 1165–1173.
- [6] A. Shaban, C.-A. Cheng, N. Hatch, and B. Boots, “Truncated back-propagation for bilevel optimization,” in *Proc. Int. Conf. Artif. Intell. Statist.*, 2019, pp. 1723–1732.
- [7] Ö. Çiçek, A. Abdulkadir, S. S. Lienkamp, T. Brox, and O. Ronneberger, “3D U-Net: Learning dense volumetric segmentation from sparse annotation,” in *Proc. Med. Image Comput. Comput.-Assist. Intervention*, 2016, pp. 424–432.
- [8] K. Zhang, Y. Li, W. Zuo, L. Zhang, L. Van Gool, and R. Timofte, “Plug-and-play image restoration with deep denoiser prior,” *IEEE Trans. Pattern Anal. Mach. Intell.*, vol. 44, no. 10, pp. 6360–6376, Oct. 2022.
- [9] J.-Y. Zhu, T. Park, P. Isola, and A. A. Efros, “Unpaired image-to-image translation using cycle-consistent adversarial networks,” in *Proc. Int. Conf. Comput. Vis.*, 2017, pp. 2223–2232.
- [10] K. Ji, J. D. Lee, Y. Liang, and H. V. Poor, “Convergence of meta-learning with task-specific adaptation over partial parameters,” *Adv. Neural Inf. Process. Syst.*, vol. 33, pp. 11 490–11 500, 2020.
- [11] F. Pedregosa, “Hyperparameter optimization with approximate gradient,” in *Proc. Int. Conf. Mach. Learn.*, 2016, pp. 737–746.
- [12] J. Lorraine, P. Vicol, and D. Duvenaud, “Optimizing millions of hyperparameters by implicit differentiation,” in *Proc. Int. Conf. Artif. Intell. Statist.*, PMLR, 2020, pp. 1540–1552.
- [13] L. Metz, B. Poole, D. Pfau, and J. Sohl-Dickstein, “Unrolled generative adversarial networks,” 2016, *arXiv:1611.02163*.
- [14] A. Brock, J. Donahue, and K. Simonyan, “Large scale GAN training for high fidelity natural image synthesis,” 2018, *arXiv: 1809.11096*.
- [15] H. Petzka, A. Fischer, and D. Lukovicov, “On the regularization of wasserstein GANs,” 2017, *arXiv: 1709.08294*.
- [16] F. Farnia and A. Ozdaglar, “Do GANs always have Nash equilibria?,” in *Proc. Int. Conf. Mach. Learn.*, 2020, pp. 3029–3039.
- [17] F. Gao, Y. Yang, J. Wang, J. Sun, E. Yang, and H. Zhou, “A deep convolutional generative adversarial networks (DCGANs)-based semi-supervised method for object recognition in synthetic aperture radar (SAR) images,” *Remote Sens.*, vol. 10, no. 6, 2018, Art. no. 846.
- [18] J. Engel, M. Hoffman, and A. Roberts, “Latent constraints: Learning to generate conditionally from unconditional generative models,” 2017, *arXiv: 1711.05772*.
- [19] S. Azadi, M. Fisher, V. G. Kim, Z. Wang, E. Shechtman, and T. Darrell, “Multi-content GAN for few-shot font style transfer,” in *Proc. IEEE/CVF Conf. Comput. Vis. Pattern Recognit.*, 2018, pp. 7564–7573.
- [20] J. Fu, K. Luo, and S. Levine, “Learning robust rewards with adversarial inverse reinforcement learning,” 2017, *arXiv: 1710.11248*.
- [21] K. Arulkumaran and D. O. Lillicrap, “A pragmatic look at deep imitation learning,” 2021, *arXiv:2108.01867*.
- [22] Y. Jiang et al., “EnlightenGAN: Deep light enhancement without paired supervision,” *IEEE Trans. Image Process.*, vol. 30, pp. 2340–2349, 2021.
- [23] D. Pfau and O. Vinyals, “Connecting generative adversarial networks and actor-critic methods,” 2016, *arXiv:1610.01945*.
- [24] Z. Xu and M. Niethammer, “DeepAtlas: Joint semi-supervised learning of image registration and segmentation,” in *Proc. 22nd Int. Conf. Med. Image Comput. Comput. Assist. Intervention*, 2019, pp. 420–429.
- [25] Y. He et al., “Learning better registration to learn better few-shot medical image segmentation: Authenticity, diversity, and robustness,” *IEEE Trans. Neural Netw. Learn. Syst.*, vol. 35, no. 2, pp. 2588–2601, Feb. 2024.
- [26] D. Tomar, B. Bozorgtabar, M. Lortkipanidze, G. Vray, M. S. Rad, and J. Thiran, “Self-supervised generative style transfer for one-shot medical image segmentation,” in *Proc. IEEE/CVF Winter Conf. Appl. Comput. Vis.*, 2022, pp. 1737–1747.

- [27] A. Zhao, G. Balakrishnan, F. Durand, J. V. Guttag, and A. V. Dalca, "Data augmentation using learned transformations for one-shot medical image segmentation," in *Proc. IEEE/CVF Conf. Comput. Vis. Pattern Recognit.*, 2019, pp. 8543–8553.
- [28] R. Liu, L. Ma, T. Ma, X. Fan, and Z. Luo, "Learning with nested scene modeling and cooperative architecture search for low-light vision," *IEEE Trans. Pattern Anal. Mach. Intell.*, vol. 45, no. 5, pp. 5953–5969, May 2023.
- [29] X. Xue, J. He, L. Ma, Y. Wang, X. Fan, and R. Liu, "Best of both worlds: See and understand clearly in the dark," in *Proc. ACM Int. Conf. Multimedia*, 2022, pp. 2154–2162.
- [30] R. Liu, Y. Liu, S. Zeng, and J. Zhang, "Towards gradient-based bilevel optimization with non-convex followers and beyond," *Adv. Neural Inf. Process. Syst.*, vol. 34, pp. 8662–8675, 2021.
- [31] R. Liu, P. Mu, X. Yuan, S. Zeng, and J. Zhang, "A general descent aggregation framework for gradient-based bi-level optimization," *IEEE Trans. Pattern Anal. Mach. Intell.*, vol. 45, no. 1, pp. 38–57, Jan. 2022.
- [32] K. Zhang, W. Zuo, S. Gu, and L. Zhang, "Learning deep CNN denoiser prior for image restoration," in *Proc. IEEE/CVF Conf. Comput. Vis. Pattern Recognit.*, 2017, pp. 3929–3938.
- [33] Z. Li, F. Zhou, F. Chen, and H. Li, "Meta-SGD: Learning to learn quickly for few-shot learning," 2017, *arXiv: 1707.09835*.
- [34] A. Nichol, J. Achiam, and J. Schulman, "On first-order meta-learning algorithms," 2018, *arXiv: 1803.02999*.
- [35] L. Franceschi, M. Donini, P. Frasconi, and M. Pontil, "A bridge between hyperparameter optimization and learning-to-learn," 2017, *arXiv: 1712.06283*.
- [36] R. Liu, J. Gao, J. Zhang, D. Meng, and Z. Lin, "Investigating bi-level optimization for learning and vision from a unified perspective: A survey and beyond," *IEEE Trans. Pattern Anal. Mach. Intell.*, vol. 44, no. 12, pp. 10 045–10 067, Dec. 2022.
- [37] L. Ma, T. Ma, R. Liu, X. Fan, and Z. Luo, "Toward fast, flexible, and robust low-light image enhancement," in *Proc. IEEE/CVF Conf. Comput. Vis. Pattern Recognit.*, 2022, pp. 5637–5646.
- [38] J. Li et al., "DSFD: Dual shot face detector," in *Proc. IEEE/CVF Conf. Comput. Vis. Pattern Recognit.*, 2019, pp. 5060–5069.
- [39] R. Liu, X. Liu, S. Zeng, J. Zhang, and Y. Zhang, "Value-function-based sequential minimization for bi-level optimization," 2021, *arXiv: 2110.04974*.
- [40] X. Mao, Q. Li, H. Xie, R. Y. Lau, Z. Wang, and S. P. Smolley, "Least squares generative adversarial networks," in *Proc. Int. Conf. Comput. Vis.*, 2017, pp. 2813–2821.
- [41] A. Krizhevsky and G. Hinton, "Convolutional deep belief networks on cifar-10," *Unpublished Manuscript*, vol. 40, no. 7, pp. 1–9, 2010.
- [42] A. Krizhevsky and G. Hinton, "Learning multiple layers of features from tiny images," *Handbook Systemic Autoimmune Dis.*, vol. 1, no. 4, 2009.
- [43] Z. Liu, P. Luo, X. Wang, and X. Tang, "Deep learning face attributes in the wild," in *Proc. Int. Conf. Comput. Vis.*, 2015, pp. 3730–3738.
- [44] M. Heusel, H. Ramsauer, T. Unterthiner, B. Nessler, and S. Hochreiter, "GANs trained by a two time-scale update rule converge to a local nash equilibrium," *Adv. Neural Inf. Process. Syst.*, vol. 30, pp. 6629–6640, 2017.
- [45] T. Miyato, T. Kataoka, M. Koyama, and Y. Yoshida, "Spectral normalization for generative adversarial networks," 2018, *arXiv: 1802.05957*.
- [46] T. Karras, S. Laine, and T. Aila, "A style-based generator architecture for generative adversarial networks," in *Proc. IEEE/CVF Conf. Comput. Vis. Pattern Recognit.*, 2019, pp. 4401–4410.
- [47] G. Balakrishnan, A. Zhao, M. R. Sabuncu, J. V. Guttag, and A. V. Dalca, "Voxelmorph: A learning framework for deformable medical image registration," *IEEE Trans. Med. Imag.*, vol. 38, no. 8, pp. 1788–1800, Aug. 2019.
- [48] X. Jia, J. Bartlett, T. Zhang, W. Lu, Z. Qiu, and J. Duan, "U-Net versus transformer: Is U-Net outdated in medical image registration?," in *Proc. Int. Workshop Mach. Learn. Med. Imag.*, 2022, pp. 151–160.
- [49] J. Chen, E. C. Frey, Y. He, W. P. Segars, Y. Li, and Y. Du, "TransMorph: Transformer for unsupervised medical image registration," *Med. Image Anal.*, vol. 82, 2022, Art. no. 102615.
- [50] S. Chen, G. Bortsova, A. G. Juárez, G. van Tulder, and M. de Bruijne, "Multi-task attention-based semi-supervised learning for medical image segmentation," in *Proc. 22nd Int. Conf. Med. Image Comput. Comput. Assist. Intervention*, 2019, pp. 457–465.
- [51] X. Chen, Y. Yuan, G. Zeng, and J. Wang, "Semi-supervised semantic segmentation with cross pseudo supervision," in *Proc. IEEE/CVF Conf. Comput. Vis. Pattern Recognit.*, 2021, pp. 2613–2622.
- [52] W. Chen, W. Wang, W. Yang, and J. Liu, "Deep retinex decomposition for low-light enhancement," in *Proc. Brit. Mach. Vis. Conf.*, 2018, pp. 155.
- [53] Y. Zhang, J. Zhang, and X. Guo, "Kindling the darkness: A practical low-light image enhancer," in *Proc. 27th ACM Int. Conf. multimedia*, 2019, pp. 1632–1640.
- [54] C. Guo et al., "Zero-reference deep curve estimation for low-light image enhancement," in *Proc. IEEE/CVF Conf. Comput. Vis. Pattern Recognit.*, 2020, pp. 1780–1789.
- [55] R. Wang, Q. Zhang, C.-W. Fu, X. Shen, W.-S. Zheng, and J. Jia, "Under-exposed photo enhancement using deep illumination estimation," in *Proc. IEEE/CVF Conf. Comput. Vis. Pattern Recognit.*, 2019, pp. 6849–6857.
- [56] K. Xu, X. Yang, B. Yin, and R. W. Lau, "Learning to restore low-light images via decomposition-and-enhancement," in *Proc. IEEE/CVF Conf. Comput. Vis. Pattern Recognit.*, 2020, pp. 2281–2290.
- [57] W. Yang, S. Wang, Y. Fang, Y. Wang, and J. Liu, "From fidelity to perceptual quality: A semi-supervised approach for low-light image enhancement," in *Proc. IEEE/CVF Conf. Comput. Vis. Pattern Recognit.*, 2020, pp. 3063–3072.
- [58] R. Liu, X. Liu, W. Yao, S. Zeng, and J. Zhang, "Towards extremely fast bilevel optimization with self-governed convergence guarantees," 2022, *arXiv: 2205.10054*.
- [59] J. Kruse, C. Rother, and U. Schmidt, "Learning to push the limits of efficient FFT-based image deconvolution," in *Proc. Int. Conf. Comput. Vis.*, 2017, pp. 4586–4594.
- [60] S. Baik, S. Hong, and K. M. Lee, "Learning to forget for meta-learning," in *Proc. IEEE/CVF Conf. Comput. Vis. Pattern Recognit.*, 2020, pp. 2379–2387.



Risheng Liu (Member, IEEE) received the BSc and PhD degrees from the Dalian University of Technology, China, in 2007 and 2012, respectively. From 2010 to 2012, he was doing research as joint PhD with robotics institute, Carnegie Mellon University. From 2016 to 2018, He was doing research as Hong Kong Scholar with the Hong Kong Polytechnic University. He is currently a full professor with the School of Software Technology, Dalian University of Technology. He was awarded the "Outstanding Youth Science Foundation" of the National Natural Science Foundation of China. His research interests include optimization, computer vision and multimedia.



Jiaxin Gao received the BS degree in applied mathematics from the Dalian University of Technology, Dalian, China, in 2018. She is currently working toward the PhD degree in software engineering with the Dalian University of Technology, Dalian. She is with the Key Laboratory for Ubiquitous Network and Service Software of Liaoning Province, Dalian University of Technology. Her research interests include computer vision, machine learning and optimization.



Xuan Liu received the BSc degree in mathematics from the Dalian University of Technology, in 2020. He is currently working toward the MPhil degree with the Department of Software Engineering, Dalian University of Technology. His research interests include computer vision, machine learning, and control and optimization.



Xin Fan (Senior Member, IEEE) received the BE and PhD degrees from Xi'an Jiaotong University, Xi'an, China, in 1998 and 2004, respectively. He was with Oklahoma State University, Stillwater, and the University of Texas Southwestern Medical Center, Dallas, from 2006 to 2009, as a post-doctoral research fellow. He joined Dalian University of Technology, Dalian, China, in 2009, where he is currently a full professor. He won the 2015 IEEE ICME Best Student Award as the corresponding author, and two papers were selected as the Finalist of the Best Paper Award at ICME 2017. His current research interests include image processing and machine vision.